Geostatistical Earth Modeling of Cyclic Depositional Facies and Diagenesis

Thomas Le Blévec, Olivier Dubrule, Cédric M. John, Gary J. Hampson

July 2, 2018

Thomas Le Blévec

t.le-blevec15@imperial.ac.uk

Earth Science and Engineering, Imperial College, London, UK

Olivier Dubrule

o.dubrule@imperial.ac.uk

Earth Science and Engineering, Imperial College, London, UK

Cédric M. John

cedric.john@imperial.ac.uk

Earth Science and Engineering, Imperial College, London, UK

Gary J. Hampson

g.j.hampson@imperial.ac.uk

Earth Science and Engineering, Imperial College, London, UK

Acknowledgements

The authors would like to thank Carl Jacquemyn and Claire Veillard for providing practical examples and contributing ideas to this paper, and the department of Earth Science and Engineering at Imperial College for a scholarship to Thomas Le Blévec. Olivier Dubrule would like to thank Total for seconding him at Imperial College London.

Abstract

In siliciclastic and carbonate reservoirs, depositional facies are often described as being organized in cyclic successions that are overprinted by diagenesis. Most reservoir modeling workflows are not able to reproduce stochastically such patterns. Herein, a novel geostatistical method is developed to model depositional facies architectures that are rhythmic and cyclic, together with superimposed diagenetic facies.

The method uses truncated Pluri-Gaussian random functions constrained by transiograms. Cyclicity is defined as an asymmetric ordering between facies, and its direction is given by a three-dimensional vector, called shift. This method is illustrated on two case studies. Outcrop data of the Triassic Latemar carbonate platform, northern Italy, are used to model shallowing-upward facies cycles in the vertical direction. A satellite image of the modern Bermuda platform interior is used to model facies cycles in the windward-to-leeward lateral direction.

As depositional facies architectures are modelled using two Gaussian random functions, a third Gaussian random function is added to model diagenesis. Thereby, depositional and diagenetic facies can exhibit spatial asymmetric relations. The method is applied in two regions of the Latemar carbonate platform that experience two different types of diagenetic transformation: syn-depositional dolomite formation, and post-depositional fracture-related diagenesis. The method can also incorporate proportion curves to model non-stationary facies proportions. This is illustrated in Cretaceous shallow-marine sandstones and mudstones, Book Cliffs, Utah, for which cyclic facies and diagenetic patterns are constrained by embedded transition probabilities.

Introduction

In reservoir modeling applications, an important step is the representation of three-dimensional facies architecture and the quantification of associated uncertainty. The geomodeling community routinely uses geostatistical methods to reach this goal

(Koltermann and Gorelick, 1996; Alabert and Modot, 1992; Pyrcz and Deutsch, 2014). However, the commonly-used geostatistical approaches have some significant limitations. For instance, geostatistical models often show the same facies successions in the upward as in the downward direction, which does not allow the representation of classic geological features such as facies cyclicity or certain types of syn-depositional diagenesis.

Modeling Cyclicity and Rhythmicity

Depositional facies in vertical successions exhibit extensive cyclicity and rhythmicity (Strasser, 1988; Goldhammer et al., 1990; Wilkinson et al., 1997; Lindsay et al., 2006; Burgess, 2016). These features are defined respectively as facies ordering (Gingerich, 1969; Hattori, 1976) and repetition of facies at intervals of constant thickness (De Boer and Wonders, 1984; House, 1985). Their origin is attributed to various controls, including relative sea level oscillations (e.g., Grotzinger, 1986), local tectonic activity (e.g., Cisne, 1986) and autogenic mechanisms. These different origins may lead to cycles and rhythms of differing lateral extent and stacking patterns, which should be reproduced by the modeling method. For example, facies cycles are commonly interpreted at reservoir scale with reference to sequence stratigraphic models, implying that they are laterally extensive (e.g., Goldhammer et al., 1990), although over such distances, some facies cycles are documented to pinch out (e.g., Egenhoff et al., 1999). In order to represent these diverse facies cycles and rhythms, reservoir-wide deterministic correlations may not be appropriate.

Diverse facies distributions are modelled by geostatistical methods, but their current implementation cannot generate facies cycles and rhythms simultaneously. For example, cyclicity quantification is possible with Markov Chain analysis (Gingerich, 1969; Hattori, 1976), but the method is originally limited to one dimension. It was later improved by Carle and Fogg (1996) who model cyclic three dimensional Earth models thanks to asymmetric transiograms. However, the method does not incorporate rhythmicity, because the transiogram models are not flexible enough to incorporate the characteristic periodic oscillations (Jones and Ma, 2001; Dubrule, 2017), called hole-effects. Facies cyclicity and rhythmicity could theoretically be modelled by Multi-Point Statistics (Strebelle, 2002), but it is challenging to include those patterns in the required three dimensional training image.

A geostatistical method has been developed recently to model simultaneously facies cyclicity and rhythmicity (Le Blévec et al., 2018), thus improving the realism of facies Earth models. The method is based on Pluri-Gaussian Simulations (Armstrong et al., 2011), constrained by facies transiograms. The facies asymmetric ordering (or cyclicity) is defined by two Gaussian random functions spatially shifted from each other, and rhythmicity of the facies succession is modelled by defining new hole-effect covariance models (Le Blévec et al., 2018).

So far, this method has only been used to model cyclicity in the vertical direction, although cyclicity can also be observed in lateral directions. Stratigraphic forward models can produce asymmetry between facies in lateral directions (Burgess et al., 2001), and such lateral facies asymmetry is also explicit within Walther's Law (e.g., Middleton, 1973). This could possibly be modelled with the shifted Pluri-Gaussian method (Le Blévec et al., 2018) by defining a spatial shift with a lateral component.

Modeling Diagenesis

Reservoir quality is not only affected by depositional facies cyclicity. Rock properties of carbonate (e.g., Bartok et al., 1981; Moore and Wade, 2013) and siliciclastic (e.g., Taylor et al., 2010) deposits are also influenced by diagenesis. Diagenetic processes give rise to depositional and diagenetic facies with a variety of geometrical relationships, which should be captured by the modeling method. Early diagenesis tends to closely follow the texture and stratal configuration of depositional facies (e.g., Ginsburg, 1957; Egenhoff et al., 1999; Peterhänsel and Egenhoff, 2008; Rameil, 2008) while late diagenesis either follow depositional features, or other structures such as faults, fractures, and karsts, thus resulting in diagenetic bodies and trends that cut across depositional facies geometries (e.g., Sharp et al., 2010; Vandeginste et al., 2013; Jacquemyn et al., 2014; Beckert et al., 2015). It is therefore highly desirable that reservoir modeling methods are flexible enough to embrace these different possibilities.

In many geostatistical studies, diagenesis is modelled as porosity or permeability variations (Wang et al., 1998; Pontiggia et al., 2010). This is a useful approach, but it cannot be applied to the representation of distinct diagenetic geobodies or of different diagenetic phases within a depositional facies. Therefore, some authors model diagenesis as a facies random field that is superimposed on the depositional facies field (Renard et al., 2008; Doligez et al., 2011; Barbier et al., 2012; Carrera et al., 2018). These authors use a version of truncated Pluri-Gaussian Simulations (Bi-PGS) developed by Renard et al. (2008), which models two facies fields with different Gaussian random functions. The depositional and diagenetic facies fields can be either independent of or correlated to each other, which allows to model depositional and diagenetic facies geometries that are either discordant or conformable. However, this method does not generate distributions of diagenetic facies that are asymmetric such as occurring preferentially towards the top or the base of depositional facies bodies.

The algorithm of Renard et al. (2008) to model diagenesis is thus extended here by including a shift between depositional and diagenetic facies fields, which allows diagenetic facies to overprint depositional facies preferentially at their top or at their base. These relationships are constrained by cross-transiograms between the two facies fields, and the method is also combined with the advancements of Le Blévec et al. (2018), so that diagenesis is modelled in the context of depositional facies cyclicity and rhythmicity.

Aims

Therefore, this paper presents a new geostatistical facies modeling method that is able to represent facies cyclicity and rhythmicity, together with diagenetic facies bodies, which have either conformable or non-conformable geometries. The structure of the paper is outlined below. First, we illustrate the concepts of cyclicity and rhythmicity and show that these concepts are captured by transiograms. Modeling of cycles and rhythms is then illustrated using: (1) synthetic facies successions; (2) facies successions from the outcropping Triassic Latemar carbonate platform of Northern Italy; and (3) lateral facies relationships on the interior of the modern Bermuda carbonate platform. Then, diagenesis is modelled by adding another Gaussian random function to the method. Three examples are modelled to illustrate the flexibility of the method: (1) syn-depositional diagenesis below hardgrounds in facies cycles of the Latemar carbonate platform; (2) early diagenetic development of concretions in shallow-marine, siliciclastic facies cycles in the Cretaceous Blackhawk Formation, Book Cliffs outcrops (Utah), in which the facies proportions are non-stationary; and (3) post-depositional diagenesis caused by localised movement of hydrothermal fluids through faults and fractures in the Latemar carbonate platform.

Quantifying Cyclicity and Rhythmicity with Transiograms

Defining Cyclicity and Rhythmicity

Although facies cyclicity and rhythmicity are commonly interpreted in sedimentary sequences, these concepts have different meanings to different authors. Formal, quantitative definitions of cyclicity and rhythmicity are needed for facies modeling, as a facies succession can be more or less ordered or exhibit more or less variability in facies thickness. Cyclicity is defined as facies ordering in a given direction (Gingerich, 1969; Hattori, 1976; Le Blévec et al., 2018), usually vertically (Fig. 1). The ordering considered here is asymmetric, which means that it differs going upwards from going downwards. For instance, in vertical shallow-marine carbonate and siliciclastic successions, facies cycles tend to be shallowing-upward (Strasser, 1988; Goldhammer et al., 1990; Lindsay et al., 2006), which is equivalent to deepening-downward.

Another commonly observed feature is that the same facies tends to appear repeatedly at intervals of constant thickness (e.g., Goldhammer et al., 1993; Lindsay et al., 2006), which defines rhythmicity (De Boer and Wonders, 1984; House, 1985; Le Blévec et al., 2018). If cyclicity and rhythmicity are both present, it implies that the facies cycles have low variability in thickness. For instance, the vertical succession in Figure 1d is cyclic and rhythmic because the facies are fully ordered and have constant thickness intervals between them. The succession illustrated in Figure 1a has non-ordered transitions between facies and also contains two facies cycles. The succession in Figure 1b also contains two facies cycles, and the blue facies is rhythmic, because intervals between occurrences of this facies have similar thickness. Figure 1c shows a cyclic and non-rhythmic facies succession, and the succession in Figure 1d is cyclic and rhythmic, because the facies are fully ordered and the blue facies is separated by intervals of constant thickness. For three-dimensional Earth models to be geologically realistic, facies cyclicity and rhythmicity must be properly modelled.

The Transiogram: a Tool to Capture Cyclicity and Rhythmicity

Standard geostatistical simulation approaches quantify geologic patterns by computing experimental variograms, modeling them mathematically and then ensuring that the variogram models are reproduced in the final simulation (Pyrcz and Deutsch, 2014). However, Carle and Fogg (1996) show that variograms are not able to quantify asymmetric cycles, and promote the use of the transiogram instead.

The transiogram gives the probability $t_{AB}(h)$ of finding a facies B at a vector h from a given facies A (Carle and Fogg, 1996; Le Blévec et al., 2018). If the two facies A and B are identical, the transiogram is referred to as an auto-transiogram, otherwise it is referred to as a cross-transiogram. Auto-transiograms and cross-transiograms are calculated experimentally and gathered in a transiogram matrix

(Fig. 2). As with variograms, the direction h is usually vertical, but it can also have a lateral component if calculated along other directions. For sedimentary facies, transiograms are commonly different in opposite directions (e.g., upward and downward) (Carle and Fogg, 1996).

Transiograms have specific properties, which are described in detail by Carle and Fogg (1996). One property is that at long distances h, $t_{AB}(h)$ tends towards the proportion of facies B. For example, Figure 2b-e shows that the transiograms tend towards the value of 0.5, which is the proportion of facies 1, and 0.25, which is the proportion of facies 2. Also, the tangent at the origin $t'_{AA}(0)$ of the auto-transiogram $t_{AA}(h)$ defines the mean length of facies A, denoted as $\overline{L_A}$ (Carle and Fogg, 1996), as shown in Figure 2b, e ($\overline{L_1}$ and $\overline{L_2}$).

Figure 2c, and 2d also show that cyclicity is captured by the behavior at the origin of the cross-transiograms (Le Blévec et al., 2018). $t'_{12}(0)$ is high while $t'_{21}(0)$ is low, which means that facies 2 tends to overlie facies 1, while facies 1 does not tend to overlie facies 2. Consequently facies 3 overlies facies 2, creating facies cycles with facies 1 at the base, facies 2 in the center and facies 3 at the top. This cyclicity is observed in the corresponding succession (Fig. 2a), which shows that facies 1 almost always transitions upward to facies 2 (except on one occasion when it transitions directly to facies 3), and facies 2 transitions upward to facies 3.

Rhythmicity is characterized by the oscillations of the transiograms or variograms (Jones and Ma, 2001; Le Blévec et al., 2018), as shown in Figure 2. The average distance separating two repetitions of a facies is given by the first maximum of the corresponding auto-transiogram, as this is associated with the highest probability of finding the same facies (Fig. 2b, e, $\overline{L_c} = 0.4$ m). It also corresponds to the first minimum of the cross-transiograms (Fig. 2c, d), which is associated with the lowest probability of finding two different facies. In this case, because there is also cyclicity, this length $\overline{L_c}$ corresponds to the average thickness of the facies cycle and is approximately the sum of the mean thicknesses of all facies present in a cycle. This also explains why the auto-transiogram of facies 2 shows the same rhythmicity (Fig. 2e) as the auto-transiogram of facies 1 (Fig. 2b). Rhythmicity can be visually verified by examining the corresponding succession (Fig. 2a), which shows that facies cycles indeed exhibit low thickness variations (thickness of approximately 0.4 m). Therefore, transiograms appear to be better suited than variograms to the quantification of cyclicity and rhythmicity.

Modeling Cyclicity and Rhythmicity with Shifted Pluri-Gaussian Simulations

Principle of Truncated Gaussian Simulations

The truncated Gaussian approach for facies modeling was first developed by Matheron et al. (1988) and is explained in detail by Armstrong et al. (2011). It has two steps: (1) first, the simulation of a continuous Gaussian random function, and then (2) the truncation of this continuous function into facies with the help of a truncation rule.

A Gaussian random function defines at every location (x, y, z) (usually in a grid) a Gaussian random variable. The Gaussian random function is controlled by its covariance model (Chiles and Delfiner, 2012). In this paper, as explained in the Appendix, Gaussian cosine covariances (with frequency parameter b) are used with scale factor noted r_z (Eq. A.4a) in the vertical direction. In lateral directions Gaussian covariances are used, with scale factors noted r_x and r_y for each principal direction (Eq. A.4a). Scale factors control the average length scale of the Gaussian random functions in the corresponding direction and b their periodicity (Le Blévec et al., 2018). Figure 3b (red curve) shows an example of a realization of a Gaussian random function Z_1 along a vertical succession (i.e., on a one-dimensional grid).

The truncation rule defines the number of facies, their proportions, and their contacts. For instance, Figure 3a shows a truncation rule with three facies, with a small area for facies 3 defined by the threshold q_2. This results in a smaller proportion of facies 3 in the corresponding vertical succession (Fig. 3b). As shown by Figure 3b, when Z_1 is higher than q_1, facies 2 is allocated, and when it reaches q_2, facies 3 is defined.

By using only one Gaussian random function, modeling is limited because each facies can only transition into one or, at most two other facies. For instance, in Figure 3 facies 1 and 3 can only transition into facies 2, while facies 2 can transition into both facies 1 and 2 upward or downward. Therefore, cyclicity cannot be modelled because there is no asymmetry associated to the simulation. Armstrong et al. (2011) extend the method to Pluri-Gaussian Simulations, and it was then modified by Le Blévec et al. (2018) to model cyclicity.

The Shifted Pluri-Gaussian Simulations Approach

Here we summarize the modeling method developed in Le Blévec et al. (2018). The method is based on Pluri-Gaussian Simulations (PGS) (Armstrong et al., 2011), which generalizes Truncated Gaussian Simulations by using several Gaussian random functions instead of just one. An example is given in Figure 4b, which shows a Pluri-Gaussian Simulation using two Gaussian random functions Z_1 and Z_2. The variations of each Gaussian random function are controlled by their respective covariance model (Eqs. A.4a and A.4b). The truncation rule applied to them is two dimensional (Fig. 4a) and defines in this example three facies separated by two thresholds q_1 and q_2, with all three facies in contact with each other. For instance, the defined facies is yellow if q_1 is smaller than Z_1 and q_2 is smaller than Z_2. The corresponding facies succession (Fig. 4b) shows no specific cyclicity, because all facies can transition into each other randomly.

In order to model cyclicity, Le Blévec et al. (2018) introduced a spatial shift α between the two Gaussian random functions. More specifically, the Gaussian random functions are correlated (or anti-correlated) to each other by a correlation coefficient β, then shifted by a vector noted α (Eq. A.3), which gives the direction of the cyclicity. This is illustrated in Figure 4c, in which the Gaussian random functions are anti-correlated ($\beta < 0$), with a small shift α oriented upward. This results, after truncation, into a highly cyclic facies succession (Fig. 4c). The upward cycle from facies 1 to facies 2 then to facies 3 is repeated almost everywhere because Z_2 tends to cross its threshold q_2 (from facies 2 to facies 3) just after Z_1 crosses its threshold q_1 (from facies 1 to facies 2), as if the truncation rule (Fig. 4a) had an anti-clockwise motion in the upward direction. The cyclicity of the succession shown in Figure 4c is confirmed by its corresponding transiograms (Fig. 2) as explained previously.

Modeling Vertical Facies Cyclicity and Rhythmicity in the Latemar Carbonate Platform

Dataset

The Triassic Latemar carbonate platform (northern Italy) is renowned for its cyclicity (Goldhammer et al., 1990; Hinnov and Goldhammer, 1991) and is thus well suited for analysis to the new method described above. Using the original data of Peterhänsel and Egenhoff (2008), part of the Upper Cyclic Facies interval has previously been modelled by Le Blévec et al. (2018) with a simplified, three-fold classification of depositional facies that is modified from Egenhoff et al. (1999). Here, the same interval is modelled in the Cimon Latemar outcrop with the full four-fold classification of depositional facies of Egenhoff et al. (1999): subtidal (e_1), intertidal (e_2), supratidal (e_3) and subaerial exposure facies (e_4). Diagenetic overprinting is at first not considered in the model described here, but models of the Latemar platform presented later include diagenetic facies. Although depositional facies are here denominated as environments of deposition, their interpretation is directly based on application of the Dunham classification to observations in thin sections (Egenhoff et al., 1999). Therefore, it is possible that they transition laterally with each other several times at the same stratigraphic level, in a mosaic-like fashion, as shown by the interpreted cross section of Peterhänsel and Egenhoff (2008). The measured sections of Peterhänsel and Egenhoff (2008) are presented in Figure 5.

As discussed by Egenhoff et al. (1999) and Peterhänsel and Egenhoff (2008), the facies tend to be organized in shallowing-upward facies cycles that comprise, from base to top, facies 1, facies 2, facies 3, facies 4. This interpreted organization is supported by logs in Figure 5. For example, the subtidal facies e_1 tends to overlie the subaerial exposure facies e_4, which defines the base of a cycle, and is generally overlain by intertidal facies e_2. However, many cycles are incomplete and lack one or more facies (Fig. 5). There is also a high number of alternations between intertidal facies e_2 and subaerial exposure facies e_4 (e.g., in log $N17$, Fig. 5). Therefore, the cyclicity of the facies succession is not perfect and this imperfect pattern should be reproduced statistically in the model. It is also noteworthy that subtidal facies e_1 and supratidal facies e_3 are never in contact (Fig. 5).

Model

The first step is to define an appropriate truncation rule based on the observed contacts between facies and their cyclicity. As the typical cycle is $e_1 \rightarrow e_2 \rightarrow e_3 \rightarrow e_4$, these facies should be arranged clockwise (or counter-clockwise) in the truncation rule. Moreover, as observed (Fig. 5), subtidal facies should not be in contact with supratidal facies. Figure 6 shows a truncation rule satisfying these constraints. The thresholds q_1, q_2 and q_3 are computed according to the proportions of the different facies (an example of how to compute the thresholds from the proportions is given in the Appendix, using Eqs. A.7, A.8 and A.9).

The next step is to find the parameters of the model (β_{12}, α_{12}, r_1, r_2, b_1, b_2) from the experimental transiograms computed from the logs. The results are shown in Figure 7 (grey points). The parameters of the method are found so that they generate theoretical transiograms that provide a good match to the experimental transiograms. The computation of a theoretical transiogram from the parameters of the method is explained in the Appendix (Eqs. A.10, A.11 and A.12). A trial-and-error test is performed on the parameters, and the ones which give the best fit between experimental and theoretical transiograms are chosen.

It is important to note that transiograms are inter-dependent and cannot be fitted individually. For instance, the first maximum of the auto-transiograms and first minimum of the cross-transiograms are related to the cycle thickness, as explained earlier (Fig. 2). Thus, one parameter such as the shift α_{12} controls the behavior of several theoretical transiograms (see Le Blévec et al., 2017, for details). Because of these relationships between transiograms, it is usually not possible to obtain a perfect fit between experimental and theoretical transiograms, and a compromise should be made based on which feature (or combination of features) is considered by the user to be more important.

The theoretical transiograms after fitting are shown in Figure 7 (black curves). The tangents at the origin of the different auto-transiograms and cross-transiograms are matched, which means that the different facies thicknesses and the contacts between them are well constrained. Therefore, the fit between experimental and theoretical transiograms is satisfactory. Subtidal facies e_1 and supratidal facies e_3 are not in contact because $t_{e_1e_3}(h)$ and $t_{e_3e_1}(h)$ both have a tangent at the origin with a very low value, which comes from the truncation rule (Fig. 6). The only significant mismatch is for the transiogram $t_{e_4e_1}(h)$, for which the tangent at the origin of the theoretical transiogram is not high enough (Fig. 7). This means that in the model, facies e_1 has less tendency to overlie facies e_4 than in the dataset.

Some rhythmic facies patterns are also captured, such as the one observed in the transiogram $t_{e_1e_1}(h)$ (Fig. 7).

The scale factors in the lateral direction r_x and r_y are chosen by visual comparison of the resulting facies models with the outcrop cross section of Peterhänsel and Egenhoff (2008). The higher their values, the larger the extent of the facies. As the facies are quite laterally extensive, the scale factors are of the order of the size of the final Earth model of depositional facies.

Simulation

The Earth model for depositional facies is now built using the above fitted parameters. The Gaussian random functions are simulated in the grid described below, and then truncated into facies. The simulations are also conditioned to the measured sections so that the facies observed in the measured sections are reproduced in the model realizations. The algorithms to perform these steps are explained in Le Blévec et al. (2018).

The number of grid cells in each direction (East, North, Z) is $(100, 10, 182)$, and the grid dimensions are (1000 m, 250 m, 9.1 m)$\sim$(0.62 mi, 820 ft, 29 ft). Hence the size of each cell is (10 m, 25 m, 5 cm)$\sim$(33 ft, 82 ft, 16 ft). The number of cells is a compromise between the desired computational speed of the simulation and the level of details at which the heterogeneities are represented. Here, a high resolution is chosen in the vertical direction, because most of the transitions between facies are vertical. The simulation is fast and several equiprobable realizations are obtained in a two or three minutes with a standard desktop PC. Two realizations are shown in Figure 8, together with the original measured sections of Peterhänsel and Egenhoff (2008), reproduced in both realizations.

Incomplete facies cyclicity, as observed in the measured sections (Fig. 5) is visible in the realizations (Fig. 8). For instance, subaerial exposure facies e_4 are not only overlain by subtidal facies e_1 at the base of each cycle, but also by intertidal facies e_2 or supratidal facies e_3. Subtidal facies e_1 and supratidal facies e_3 are not in contact, as defined by the truncation rule (Fig. 6). Laterally, facies transition randomly into each other because no lateral transition constraint is given. This aspect of the Earth model realizations can be improved by using conceptual knowledge of the platform-interior facies architecture, leading to Earth models that exhibit lateral facies cyclicity or non-stationarity, as illustrated below.

For model validation, the transiograms are computed in three realizations of the simulation and shown in Figure 7 (thin grey curves). Most transiograms of the realizations are a good fit to the experimental and theoretical transiograms, which shows that the Earth models are geologically realistic. Some mismatches also appear, for instance in $t_{e_2e_2}(h)$, for which it seems that the realizations have a higher plateau than the model. However, these statistical variations are not systematic and are common with stochastic simulations (Chiles and Delfiner, 2012).

Extension to Lateral Cyclicity

Lateral facies cyclicity can be observed in modern environments or generated by forward stratigraphic modeling (Burgess et al., 2001). Tidal-flat and reef islands deposits in modern shallow-water carbonate environments can exhibit lateral directionality, induced by currents in the water column, which results in lateral and vertical facies cyclicity (e.g., Burgess et al., 2001). The method developed here models such vertical and lateral facies cyclicity by adding a lateral component to the shift α between the Gaussian random functions. This procedure is demonstrated using a satellite image of reef islands in the interior of the modern Bermuda platform, which was first described by Verrill (1907) (Fig. 9a). The reef island deposits show a lateral facies asymmetry, with a typical facies cycle comprising reef, backreef, and lagoonal facies (after Jordan Jr, 1973). Although there are no data describing the vertical facies succession, we assume that Walther's law (Middleton, 1973) is followed, such that the lateral facies transitions are equivalent to the vertical facies transitions. This equivalence is modeled by incorporating the lateral component into the shift vector.

One unconditional (no vertical sections are matched) realization of an Earth model for facies distribution is shown in Figure 9c, along with the model truncation rule (Fig. 9b). The three modelled facies are in contact, and lateral facies cyclicity similar to that observed in the satellite image is generated. The vertical cyclicity is such that reef facies overlie backreef facies (Fig. 9c). The combination of lateral and vertical facies cyclicity results in an overall eastward progradation of reef islands. Therefore, the shift controls the movement over time of the facies belts and bodies. For instance, if the shift was oriented to the west, then this would be the direction of progradation. If the shift was purely vertical, there would only be aggradation. Due to the lateral component of the shift, Walther's Law is respected in the model.

Modeling Diagenesis with Shifted Pluri-Gaussian Simulations

Siliciclastic and, particularly, carbonate reservoirs are widely documented to undergo extensive diagenetic modification during deposition and subsequent burial, which modifies their petrophysical properties (Moore and Wade, 2013). Therefore, it is important to provide a flexible modeling method for diagenetic overprinting of depositional facies that can mimic patterns resulting from multiple diagenetic events, in order to capture the impact on hydrocarbon recovery. Diagenesis can follow the original depositional fabric in some cases, but can also be templated by faults and fractures and thus cross-cut depositional facies. A novel method able to model these two end members, based on the Shifted Pluri-Gaussian Simulations is presented. By adding a third Gaussian function that controls diagenetic facies, the method co-simulates a depositional facies field and a diagenetic facies field. The shifts between the three Gaussian random functions allows the user to model asymmetric relations between diagenetic and depositional facies.

Modeling Syn-Depositional Diagenesis: Revisiting the Latemar Carbonate Platform

Syn-Depositional Diagenesis in the Latemar Platform

Previously we modelled the depositional facies of the Latemar carbonate platform using the measured sections of Peterhänsel and Egenhoff (2008) as input data. However, the studies of Egenhoff et al. (1999) and Peterhänsel and Egenhoff (2008) also show that diagenesis affect these facies. Tepee structures, dolomitization and caliche crusts suggest an early diagenetic overprinting.

The measured sections of Peterhänsel and Egenhoff (2008) are again chosen as data for the model. These sections show two diagenetic facies: completely dolomitized crusts and partial dolomitization, which overprint different depositional facies (Fig. 10). The dolomitic crust diagenetic facies only occurs in conjunction with subaerial exposure depositional facies, while the partially dolomitized diagenetic facies occurs in conjunction with intertidal and (marginally) supratidal depositional facies. This observation from vertical measured sections is supported by the interpreted lateral correlations of Peterhänsel and Egenhoff (2008), in which the dolomitic crust diagenetic facies transitions laterally only into subaerial exposure depositional facies. Table 1 shows the proportions of each diagenetic facies within each depositional facies.

Model

In the Earth model realizations shown in Figure 8, depositional facies were modelled using two Gaussian random functions. If diagenetic facies were included in the corresponding two dimensional truncation rule (Fig. 6), they would necessarily have geometrical properties similar to those of depositional facies. Adding a third Gaussian random function as a third dimension in the truncation rule gives a greater flexibility to represent diagenetic facies geometries and their relations with depositional facies. Moreover, diagenesis can then be modelled as a superimposed facies field that overprints the depositional facies as explained in Renard et al. (2008).

A three dimensional truncation rule for the Latemar platform is thus defined in Figure 11. The truncation rule for the depositional facies is the same as that shown in Figure 6. The third Gaussian random function defines two diagenetic facies: dolomitic crust d_1 (which overprints subaerial exposure depositional facies e_4) and partial dolomite d_2 (which overprints intertidal and supratidal depositional facies e_2 and e_3). Depositional facies e_1 is not affected by diagenesis. The thresholds q controlling the proportions of diagenetic facies within depositional facies are computed from Table 1, as explained in the Appendix (Eq. A.7). For example, diagenetic facies d_2 is more abundant in depositional facies e_2 than in depositional facies e_3, and so its area is larger in the truncation rule (Fig. 11).

Once the truncation rule is chosen, the experimental transiograms of diagenetic facies are fitted with the parameters of the method, as described previously. Cross-transiograms between depositional and diagenetic facies are fitted first, because they are controlled by a smaller number of parameters: α_{13}, β_{13}, α_{23} and β_{23} (Eq. A.3). These parameters define the relations of the first two Gaussian random functions Z_1 and Z_2 with the third Gaussian random function Z_3 and thus control relations between depositional facies and diagenetic facies. These cross-transiograms have different properties from usual cross-transiograms because they relate to two superimposed facies fields, for which facies can both be present at the same location. Therefore, their value at a distance $h = 0$ is not 0 but the probability of finding the two facies types at the same location (Table 1). The fit between theoretical transiograms (black curves, Eq. A.11) and experimental transiograms (grey points) of depositional facies and diagenetic facies is shown in Figure 12.

For most transiograms, the experimental curve at the first distance step is commonly higher than the theoretical curve (Fig. 12). This is due to the small number of data points, because there are few occurrences of diagenetic facies in the measured sections (Fig. 10), thus causing the transiograms to be statistically unreliable. However, it is worth noting that the theoretical transiograms generally show reasonable behaviors at the origin. For instance, the tangent at the origin of transiogram $t_{d_1e_1}(h)$ has a high value (Fig. 12), which shows that subtidal depositional facies tends to overlie dolomitic crust diagenetic facies, as observed in the measured sections (Fig. 10). This spatial relationship supports the facies cyclicity of the model, because the dolomitic crust diagenetic facies is present in the subaerial exposure depositional facies, which are themselves overlain by subtidal depositional facies. Similarly the high value of the tangent at the origin of transiogram $t_{d_2e_4}(h)$ shows that subaerial exposure depositional facies tends to occur above partial dolomite diagenetic facies, which is also observed in the measured sections (Fig. 10). The transiograms thus confirm that the method is able to capture asymmetry between depositional and diagenetic facies, so that diagenetic facies are ordered with respect to the depositional facies.

As stated above, the cross-transiograms between depositional facies and diagenetic facies are not equal to zero for a zero distance. For instance transiogram $t_{d_1e_4}(h)$ starts at a value close to 1 (Fig. 12) because the dolomitic crust diagenetic facies d_1 is only present in the subaerial exposure diagenetic facies e_4. The cross-transiogram then decreases abruptly, which suggests that units of the subaerial exposure diagenetic facies are thin, which is consistent with the measured sections (Fig. 10). Finally, rhythmicity, although not very pronounced, is captured in transiograms $t_{d_2e_1}(h)$ and $t_{d_2e_2}(h)$ (Fig. 12). This suggests that partial dolomite diagenetic facies d_2 is separated from subtidal depositional facies e_1 by a nearly constant thickness of 0.3 m and that partial dolomite diagenetic facies d_2 is separated from intertidal depositional facies e_2 by a nearly constant thickness of 1 m (i.e., the first maxima of transiograms $t_{d_2e_1}(h)$ and $t_{d_2e_2}(h)$; Figure 12).

The auto- and cross-transiograms of the diagenetic facies themselves are now fitted using the same procedure. The parameters controlling these transiograms are the parameters of the third covariance r_3 and b_3 (Eq. A.5), and all the other parameters mentioned above, which are left unchanged. They control the spatial properties of Z_3 and thus the geometries of diagenetic facies. Figure 13 shows the fit between experimental and theoretical transiograms. The method is able to capture the asymmetry of cross-transiograms between the two diagenetic facies as $t_{d_2d_1}(h)$ and $t_{d_1d_2}(h)$, showing that the dolomitic crust diagenetic facies d_1 tends to overlie the partial dolomite diagenetic facies d_2, and the modelled transiograms are able to match exactly this behavior at the origin (Fig. 13). Theoretical auto-transiograms $t_{d_1d_1}(h)$ and $t_{d_2d_2}(h)$ also exhibit the correct behavior at the origin, which confirms that the mean thicknesses of these diagenetic facies are well constrained (Fig. 13).

This section has shown the value of the method for capturing complex transiograms between depositional facies and diagenetic facies. Shifts α_{13} and α_{23} play an important role, which emphasizes the value of incorporating asymmetry in the modeling of syn-depositional diagenetic patterns.

Simulation

The simulation is performed as for previously described models (e.g., Figure 8), with the added third Gaussian random function. Two realizations of the Earth model showing diagenetic facies superimposed on depositional facies are shown in Figure 14. Both realizations honor the data along the measured sections (e.g., long measured section N22; Figure 14), but differ away from them (e.g., in the volume above measured section N22; Figure 14).

To verify that the resulting simulations honor the data statistics, transiograms are computed on three realizations (thin grey curves in Figure 12 and Figure 13). The simulated transiograms match the experimental transiograms quite well, even better than the theoretical transiograms. For instance, transiograms $t_{d_2e_2}(h)$ for the realizations reproduce the complex hole-effect observed in the data (Fig. 12). Similarly, transiogram $t_{d_2d_2}(h)$ of the realizations follows the experimental transiogram more closely than the theoretical transiogram (Fig. 13). This could be due to the conditioning of the simulation, which provides significant constraints on the Earth models.

Modeling syn-depositional diagenesis in non-stationary shallow-marine deposits, Book Cliffs, Utah

The Upper Cretaceous Spring Canyon Member of the Blackhawk Formation, which is exposed in the Book Cliffs (Utah), consists of shallow-marine, wave-dominated shoreface sandstones that contain overprinting diagenetic features such as carbonate-cemented concretions and leached zones (whitecaps) (Van Wagoner et al., 1990; Kamola and Huntoon, 1995; Hampson and Storms, 2003; Taylor et al., 2004). Due to their large lateral extent, the deposits display non-stationary facies proportions from proximal to distal. Herein we model the outcrop dataset to show the flexibility of the method and highlight the use of embedded transition probabilities in a non-stationary context.

Dataset

The nine measured sections reported by Taylor et al. (2004) are used here, and the facies classification is simplified into three depositional facies: distal lower shoreface heteroliths and offshore mudstones (E_1), proximal lower shoreface sandstones (E_2) and foreshore and upper shoreface sandstones (E_3). There are also two diagenetic facies: carbonate cement D_1 and leached sandstones ("whitecaps") D_2, in which carbonate material has been removed via syn-depositional diagenesis. Table 2 shows the proportion of each diagenetic facies within the different depositional facies, based on measured sections with this facies classification (Fig. 15).

No cyclicity is observed between depositional facies. Facies proportions in each measured section (represented by pie charts in Figure 15) show that from west (proximal) to east (distal), the proportion of depositional facies E_3 decreases while that of depositional facies E_1 increases. Vertical facies proportion curves show that depositional facies E_3 is only present at the top of the Spring Canyon Member in the area sampled by the measured sections. Diagenetic facies are also non-stationary because their distribution is controlled by the distribution of depositional facies (Table 2).

Modeling Non-Stationary Facies Proportions

As described above, facies proportions vary systematically over the dataset to be modelled (Fig. 15). Therefore, the final Earth model should account for these variations. This is achieved by estimating the proportions of each facies in each cell of the Earth model. (Armstrong et al., 2011; D'Or et al., 2017). First, the proportions of each facies are computed at each horizontal level from all the measured sections to give vertical facies proportion curves (Fig. 15). The vertical proportion curves are then smoothed with a moving average algorithm to remove random variations, as described in White et al. (2003). Then, the proportions of each facies are computed at each vertical measured section (pie charts of Figure 15). Finally, at each grid cell intersecting a measured section, the proportion of each facies is calculated by averaging the proportion given by the vertical proportion curve with the proportion of the facies at the measured section.

A procedure to interpolate these facies proportions between measured sections is then required. Here this is achieved by lateral simple kriging interpolation (Chiles and Delfiner, 2012) using a Gaussian covariance with a large scale factor and a mean chosen as the global proportion of each facies. Once the proportions of each facies have been calculated for every cell of the model, they are transformed into thresholds for the Gaussian random functions according to the same procedure used for the models presented earlier (Appendix, Eq. A.8).

The Model

The truncation rule can be inferred from the observation of facies contacts in the measured sections (Fig. 15). Because of the facies distribution's non-stationarity, the truncation rule is different in every cell and depends on the cell's facies proportion. Therefore, a general truncation rule is first defined in Figure 16, which is then adapted to the local facies proportions in the different cells of the Earth model (Fig. 16). The foreshore and upper shoreface sandstone depositional facies (E_3) and distal lower shoreface heteroliths and offshore mudstone depositional facies (E_1) are not in contact, because of a limited presence of foreshore and upper shoreface sandstones (which occur only five times in the measured sections) and non stationarity (Fig. 15). However, there is no reason why these facies should not be in contact away from the measured sections, and the global truncation rule is thus defined to allow this contact relationship (Fig. 16). The carbonate cement diagenetic facies (D_1) and leached sandstone diagenetic facies (D_2) are respectively present in the proximal lower shoreface sandstone depositional facies (E_2) and both the proximal lower shoreface sandstone depositional facies and the foreshore and upper shoreface sandstone depositional facies (E_2, E_3) (Fig. 16).

Transiograms are not fitted here because their behavior is strongly influenced by non stationarity, especially at long distances (Armstrong et al., 2011). However, embedded transition probabilities (Krumbein and Dacey, 1969) are not much affected by non stationarity because they just measure facies juxtapositions. They can be deduced from the parameters of the model by taking the derivative at the origin of the transiograms (Eq. A.13). Thus, they are compared to the experimental embedded transitions computed from the measured sections in order to infer the parameters α_{12} and β_{12}. The experimental (red) and model (blue) embedded matrix for the three depositional facies after fitting is

$$R_{logs/model} = \begin{bmatrix} E_1 & E_2 & E_3 \\ 0 & 1.0/0.63 & 0.0/0.36 \\ 0.72/0.79 & 0 & 0.28/0.23 \\ 0.0/0.15 & 1.0/0.85 & 0 \end{bmatrix}. \quad (1)$$

The matrix shows that foreshore and upper shoreface sandstones (E_3) and distal lower shoreface heteroliths and offshore mudstones (E_1) are not in contact in the measured sections because their embedded probability is zero, while in the model they can be in contact (r_{31}=0.15, r_{13} = 0.36) according to the truncation rule (Fig. 16). The embedded transitions from proximal lower shoreface sandstones (E_2) to the other depositional facies are similar in the model and in the measured sections.

In order to constrain the vertical component of the scale factors r_1 and r_2, the thicknesses of the depositional facies are computed in the measured sections and matched with the theoretical thicknesses, which are obtained from the derivative at the origin of the auto-transiograms (Carle and Fogg, 1996). The resulting theoretical thicknesses for the three depositional facies E_1, E_2, and E_3 are respectively 1.3 m, 0.8 m, and 0.5 m, while the experimental thicknesses computed from the measured sections are 1.4 m, 0.8 m, and 0.6 m, which is a good match.

Embedded transition probabilities between the diagenetic facies are not shown because they are simply not in contact with each other. The vertical scale factor r_3 is chosen to be similar to r_1 and r_2 because diagenetic facies have a similar thickness to depositional facies. Lateral components of the scale factors r_1, r_2 and r_3 are chosen by visual comparison of the resulting Earth model realizations and the correlation panel between measured sections of Taylor et al. (2004). The depositional facies have a large lateral extent, of the same order as the west-to-east lateral extent of the Earth model.

Simulation

The number of cells in the grid in each direction is 100 (west-to-east), 20 (north-to-south), 566 (height) and the dimensions of the grid are 20 km (∼12.4 mi) (west-to-east), 5 km (∼3.1 mi) (north-to-south), 56 m (∼184 ft) (height). The simulations are conditioned to the measured sections with the procedure outlined in Le Blévec et al. (2018).

Two realizations of the resulting Earth model are shown in Figure 17. It is clear that the realizations are non-stationary as, for instance, the proportion of foreshore and upper shoreface sandstone depositional facies (E_3) decreases towards the west. Leached sandstone diagenetic facies (D_2) also exhibit a decreasing proportion towards the west, because they are constrained by the presence of foreshore and upper shoreface sandstone depositional facies (E_3) (Table 2).

As a post-validation step, embedded transition probabilities are computed in three resulting realizations and averaged, to give the embedded matrix of transition probabilities

$$R_{simu} = \begin{bmatrix} E_1 & E_2 & E_3 \\ 0 & 0.75 & 0.25 \\ 0.79 & 0 & 0.21 \\ 0.06 & 0.94 & 0 \end{bmatrix}. \tag{2}$$

This matrix matches the embedded matrix computed from the measured sections (Eq. 1), although foreshore and upper shoreface sandstone depositional facies (E_3)

and distal lower shoreface heteroliths and offshore mudstone depositional facies (E_1) are in contact, as discussed above.

Towards Modeling Post-depositional Hydrothermal Diagenesis

Post-depositional hydrothermal diagenesis is commonly observed at outcrop (Jacquemyn et al., 2014; Vandeginste et al., 2013; Beckert et al., 2015) and interpreted in the subsurface (Davies and Smith Jr, 2006; Smith Jr, 2006). Hydrothermal diagenesis produces diagenetic bodies that are discordant with strata and instead follow faults, fractures and other structures. Depositional facies may differ in their permeability, such that hydrothermal fluids can also flow laterally away from faults and fractures along relatively permeable facies belts and bodies, thus creating so-called "Christmas tree" geometries (Beckert et al., 2015). For example, outcrops of the Latemar carbonate platform in Valsorda valley exhibit such fracture-related hydrothermal diagenesis, which generate dolomite that is distributed along and nearby to fractures (Fig. 18, after Jacquemyn et al. (2014)).

This type of dolomitization can be represented in our method thanks to the third Gaussian random function covariance $\rho_3(h)$, which can have a different anisotropy from that of the two other Gaussian random functions covariances (Eq. A.4c). An unconditional realization of such a model is shown in Figure 19. The third Gaussian random function is modelled independently from the two other Gaussian random functions ($\beta_{13} = \beta_{23} = 0$), so that the geometries of diagenetic dolomite bodies cut across depositional facies geometries. The truncation rule controls the extent of dolomite within each depositional facies (Fig. 19). Depositional facies E_3 contains more dolomite than depositional facies E_2, because the volume of dolomitized facies D_{E_3} in the truncation rule is larger that of dolomitized facies D_{E_2}. On the contrary, depositional facies E_1 is not affected by diagenesis.

The Earth model realization (Fig. 19) shows that depositional facies tend to be organized in shallowing-upward asymmetric cycles and diagenetic dolomite bodies cut across them. The dolomite diagenetic facies (D_{E_2} and D_{E_3}) is more abundant in depositional facies E_3 than in depositional facies E_2, and is not present at all in depositional facies E_1, as constrained by the truncation rule.

Conclusion and Recommendations

The new method proposed in this paper models depositional and diagenetic facies fields with cyclic and rhythmic patterns. The method is based on a novel Pluri-Gaussian approach, using three dimensional truncation rules and Gaussian random functions shifted from each other. Qualitative information and concepts are used to construct the truncation rule, and the other parameters of the method are defined by fitting the experimental auto- and cross- transiograms. The resulting models show that a combination of lateral and vertical facies cyclicity can be used to generate aggradational and progradational facies geometries.

In addition, we model depositional facies overprinted by cross-cutting or conformable diagenesis. This is possible because the three Gaussian random functions are spatially shifted from each other, and depositional and diagenetic facies are ordered according to the cross-transiograms.

The method has also shown its capability to model non-stationary facies proportions, which is a predominant feature in datasets that contain pronounced proximal-to-distal or axial-to-marginal facies trends. In such cases, it is not appropriate to use transiograms to constrain the parameters of the method. Instead, it is suggested to use embedded transition probabilities, because non stationarity does not significantly impact facies juxtapositions.

The method significantly improves the capability of geostatistical Earth models to represent geologically realistic facies architectures, and thus can lead to more realistic geostatistical reservoir models and more accurate hydrocarbon production forecasts.

A Appendix: Shifted Pluri-Gaussian Model

The model developed in this paper is an extension of that developed by Le Blévec et al. (2018). Three Gaussian random functions Z_1, Z_2, Z_3 are correlated and shifted relative to each other and truncated into facies according to a truncation rule (e.g., Figure 11). The first two Gaussian random functions control depositional facies while the third Gaussian random function controls diagenetic facies. A shifted version of the linear model of co-regionalization (Wackernagel, 2003) is used

$$\begin{cases} Z_1(x) = Y_1(x), \\ Z_2(x) = \beta_{12}\ Y_1(x+\alpha_{12}) + \sqrt{1-\beta_{12}^2}\ Y_2(x), \\ Z_3(x) = \beta_{13}\ Y_1(x+\alpha_{13}) + \beta_{23}\ Y_2(x+\alpha_{23}) + \sqrt{1-\beta_{13}^2-\beta_{23}^2}\ Y_3(x), \end{cases} \tag{A.3}$$

where $-1 < \beta_{ij} < 1$ are the correlations coefficients between $Y_i(x+\alpha_{ij})$ and $Z_j(x)$, α_{ij} being the shifts, and Y_1, Y_2, Y_3 are uncorrelated Gaussian random functions with respective covariances in three dimensions

$$\rho_1(h_x, h_y, h_z) = \exp\Big(-\frac{h_x^2}{r_{1x}^2} - \frac{h_y^2}{r_{1y}^2} - \frac{h_z^2}{r_{1z}^2}\Big)\ \cos(b_1\ h_z), \tag{A.4a}$$

$$\rho_2(h_x, h_y, h_z) = \exp\Big(-\frac{h_x^2}{r_{2x}^2} - \frac{h_y^2}{r_{2y}^2} - \frac{h_z^2}{r_{2z}^2}\Big)\ \cos(b_2\ h_z), \tag{A.4b}$$

$$\rho_3(h_x, h_y, h_z) = \exp\Big(-\frac{h_x^2}{r_{3x}^2} - \frac{h_y^2}{r_{3y}^2} - \frac{h_z^2}{r_{3z}^2}\Big)\ \cos(b_3\ h_z), \tag{A.4c}$$

with $r_i = (r_{ix}, r_{iy}, r_{iz})$ the scale factors in three dimensions and b_i the frequencies of the cosine functions. Therefore, the auto-covariances of the three Gaussian random functions Z_1, Z_2, Z_3 are respectively

$$\begin{cases} \rho_{Z_1}(h) = \rho_1(h), \\ \rho_{Z_2}(h) = \beta_{12}^2\ \rho_1(h) + (1-\beta_{12}^2)\ \rho_2(h), \\ \rho_{Z_3}(h) = \beta_{13}^2\ \rho_1(h) + \beta_{23}^2\ \rho_2(h) + (1-\beta_{13}^2-\beta_{23}^2)\ \rho_3(h), \end{cases} \tag{A.5}$$

and the cross-covariances between them

$$\begin{cases} \rho_{Z_1Z_2}(h) = \beta_{12}\ \rho_1(h+\alpha_{12}), \\ \rho_{Z_1Z_3}(h) = \beta_{13}\ \rho_1(h+\alpha_{13}), \\ \rho_{Z_2Z_3}(h) = \beta_{12}\ \beta_{13}\ \rho_1(h+\alpha_{13}-\alpha_{12}) + \beta_{23}\ \sqrt{1-\beta_{12}^2}\ \rho_2(h+\alpha_{23}). \end{cases} \tag{A.6}$$

These covariances are used to derive the thresholds of the Gaussian random functions from the proportions of the different facies. For instance, let us determine the threshold q_{d_1} of the third Gaussian random function Z_1 that controls the proportion of the facies d_1 (Fig. 11)

$$p_{d1} = Pr[Z_1(x) > q_1, Z_2(x) < q_3, Z_3(x) > q_{d1}], \tag{A.7}$$

which can be re-written by integration of the multi-variate Gaussian density $G_\Sigma(u, v, w)$

$$p_{d1} = \int_{q_1}^{\infty} \int_{-\infty}^{q_2} \int_{q_{d1}}^{\infty} G_\Sigma(u,v,w)\ du\ dv\ dw, \tag{A.8}$$

with Σ the covariance matrix

$$\Sigma = \begin{bmatrix} 1 & \rho_{Z_1Z_2}(0) & \rho_{Z_1Z_3}(0) \\ \rho_{Z_1Z_2}(0) & 1 & \rho_{Z_2Z_3}(0) \\ \rho_{Z_1Z_3}(0) & \rho_{Z_2Z_3}(0) & 1 \end{bmatrix}. \tag{A.9}$$

Equation A.8 is then solved numerically with the algorithm of Genz (1992). The same methodology is applied to compute theoretical transiograms (Fig. 7). For instance, let us examine the transiogram between facies e_1 and e_2 (Fig. 11)

$$t_{e1e2}(h) = \frac{Pr[Z_1(x) < q_1, Z_2(x) < q_2, Z_1(x+h) < q_1, Z_2(x+h) > q_2]}{p_{e1}}, \tag{A.10}$$

which can be re-written by integration of Gaussian multi-variate density

$$t_{e1e2}(h) = \frac{1}{p_{e1}} \int_{-\infty}^{q_1} \int_{-\infty}^{q_2} \int_{-\infty}^{q_1} \int_{q_2}^{\infty} G_{\Sigma(h)}(u, v, w, y)\ du\ dv\ dw\ dy, \tag{A.11}$$

with $\Sigma_{(h)}$ the Gaussian covariance matrix

$$\Sigma(h) = \begin{bmatrix} 1 & \rho_{Z_1Z_2}(0) & \rho_{Z_1}(h) & \rho_{Z_1Z_2}(h) \\ \rho_{Z_1Z_2}(0) & 1 & \rho_{Z_2Z_1}(h) & \rho_{Z_2}(h) \\ \rho_{Z_1}(h) & \rho_{Z_2Z_1}(h) & 1 & \rho_{Z_1Z_2}(0) \\ \rho_{Z_1Z_2}(h) & \rho_{Z_2}(h) & \rho_{Z_1Z_2}(0) & 1 \end{bmatrix}. \tag{A.12}$$

Equation A.11 is then solved numerically with the algorithm of Genz (1992) and the same methodology is applied for the other transiograms. The embedded transition probabilities are computed from the transiograms as follows

$$r_{ij} = -\frac{t'_{ij}(0)}{t'_{ii}(0)}. \tag{A.13}$$

References

Alabert F, Modot V (1992) Stochastic models of reservoir heterogeneity: Impact on connectivity and average permeabilities. In: SPE Annual Technical Conference and Exhibition, 4-7 October, Washington, D.C, Society of Petroleum Engineers

Armstrong M, Galli A, Beucher H, Loc'h G, Renard D, Doligez B, Eschard R, Geffroy F (2011) PluriGaussian simulations in geosciences. Berlin, Springer Science & Business Media

Barbier M, Hamon Y, Doligez B, Callot JP, Floquet M, Daniel JM (2012) Stochastic joint simulation of facies and diagenesis: a case study on early diagenesis of the

Madison formation (Wyoming, USA). Oil & Gas Science and Technology–Revue d'IFP Energies nouvelles 67(1):123–145

Bartok P, Reijers T, Juhasz I (1981) Lower Cretaceous Cogollo Group, Maracaibo Basin, Venezuela: sedimentology, diagenesis, and petrophysics. AAPG Bulletin 65(6):1110–1134

Beckert J, Vandeginste V, John CM (2015) Exploring the geological features and processes that control the shape and internal fabrics of late diagenetic dolomite bodies (Lower Khuff equivalent–Central Oman Mountains). Marine and Petroleum Geology 68:325–340

Burgess P, Wright V, Emery D (2001) Numerical forward modelling of peritidal carbonate parasequence development: implications for outcrop interpretation. Basin Research 13(1):1–16

Burgess PM (2016) Identifying ordered strata: Evidence, methods, and meaning. Journal of Sedimentary Research 86(3):148–167

Carle SF, Fogg GE (1996) Transition probability-based indicator geostatistics. Mathematical geology 28(4):453–476

Carrera MFL, Barbier M, Le Ravalec M (2018) Accounting for diagenesis overprint in carbonate reservoirs using parametrization technique and optimization workflow for production data matching. Journal of Petroleum Exploration and Production Technology pp 1–15

Chiles JP, Delfiner P (2012) Geostatistics: modeling spatial uncertainty, vol 497. Hoboken, John Wiley & Sons

Cisne JL (1986) Earthquakes recorded stratigraphically on carbonate platforms. Nature 323(6086):320

Davies GR, Smith Jr LB (2006) Structurally controlled hydrothermal dolomite reservoir facies: An overview. AAPG bulletin 90(11):1641–1690

De Boer P, Wonders A (1984) Astronomically induced rhythmic bedding in Cretaceous pelagic sediments near Moria (Italy). Milankovitch and climate pp 177–190

Doligez B, Hamon Y, Barbier M, Nader F, Lerat O, Beucher H (2011) Advanced workflows for joint modelling of sedimentary facies and diagenetic overprint, impact on reservoir quality. Proceedings - SPE Annual Technical Conference and Exhibition, 3 pp 2003–2016

D'Or D, David E, Walgenwitz A, Pluyaud P, Allard D (2017) Non stationary pluri-Gaussian simulations with auto-adaptative truncation diagrams using the cart algorithm. In: 79th EAGE Conference and Exhibition 2017

Dubrule O (2017) Indicator variogram models: Do we have much choice? Mathematical Geosciences 49(4):441–465

Egenhoff SO, Peterhänsel A, Bechstädt T, Zühlke R, Grötsch J (1999) Facies architecture of an isolated carbonate platform: tracing the cycles of the Latemar (Middle Triassic, northern Italy). Sedimentology 46(5):893–912

Genz A (1992) Numerical computation of multivariate normal probabilities. Journal of computational and graphical statistics 1(2):141–149

Gingerich PD (1969) Markov analysis of cyclic alluvial sediments. Journal of sedimentary research 39(1)

Ginsburg RN (1957) Early diagenesis and lithification of shallow-water carbonate sediments in south Florida. Special Publications of SEPM 5

Goldhammer R, Dunn P, Hardie L (1990) Depositional cycles, composite sea-level changes, cycle stacking patterns, and the hierarchy of stratigraphic forcing: examples from Alpine Triassic platform carbonates. Geological Society of America Bulletin 102(5):535–562

Goldhammer R, Lehmann P, Dunn P (1993) The origin of high-frequency platform carbonate cycles and third-order sequences (Lower Ordovician El Paso Gp, west

Texas): constraints from outcrop data and stratigraphic modeling. Journal of Sedimentary Research 63(3)

Grotzinger JP (1986) Evolution of Early Proterozoic passive-margin carbonate platform, rocknest formation, wopmay orogen, Northwest Territories, Canada. Journal of Sedimentary Research 56(6)

Hampson GJ, Storms JE (2003) Geomorphological and sequence stratigraphic variability in wave-dominated, shoreface-shelf parasequences. Sedimentology 50(4):667–701

Hattori I (1976) Entropy in Markov chains and discrimination of cyclic patterns in lithologic successions. Journal of the International Association for Mathematical Geology 8(4):477–497

Hinnov LA, Goldhammer RK (1991) Spectral analysis of the Middle Triassic Latemar limestone. Journal of Sedimentary Research 61(7)

House MR (1985) A new approach to an absolute timescale from measurements of orbital cycles and sedimentary microrhythms. Nature 315(6022):721

Jacquemyn C, El Desouky H, Hunt D, Casini G, Swennen R (2014) Dolomitization of the Latemar platform: Fluid flow and dolomite evolution. Marine and Petroleum Geology 55:43–67

Jones TA, Ma YZ (2001) Teacher's aide: geologic characteristics of hole-effect variograms calculated from lithology-indicator variables. Mathematical Geology 33(5):615–629

Jordan Jr CF (1973) Carbonate facies and sedimentation of patch reefs off Bermuda. AAPG Bulletin 57(1):42–54

Kamola DL, Huntoon JE (1995) Repetitive stratal patterns in a foreland basin sandstone and their possible tectonic significance. Geology 23(2):177–180

Koltermann CE, Gorelick SM (1996) Heterogeneity in sedimentary deposits: A review of structure-imitating, process-imitating, and descriptive approaches. Water Resources Research 32(9):2617–2658

Krumbein WC, Dacey MF (1969) Markov chains and embedded Markov chains in geology. Journal of the International Association for Mathematical Geology 1(1):79–96

Le Blévec T, Dubrule O, John CM, Hampson GJ (2017) Modelling asymmetrical facies successions using pluri-Gaussian simulations. In: Geostatistics Valencia 2016, Springer, pp 59–75

Le Blévec T, Dubrule O, John CM, Hampson GJ (2018) Geostatistical modelling of cyclic and rhythmic facies architectures. Mathematical Geosciences URL https://doi.org/10.1007/s11004-018-9737-y

Lindsay RF, Cantrell DL, Hughes GW, Keith TH, Mueller III HW, Russell SD (2006) Ghawar Arab-D reservoir: widespread porosity in shoaling-upward carbonate cycles, Saudi Arabia. AAPG Special Volumes

Matheron G, Beucher H, de Fouquet C, Galli A, Ravenne C (1988) Simulation conditionnelle à trois faciès dans une falaise de la formation du Brent. Sciences de la Terre, Série Informatique Géologique 28:213–249

Middleton GV (1973) Johannes Walther's law of the correlation of facies. Geological Society of America Bulletin 84(3):979–988

Moore CH, Wade WJ (2013) Carbonate reservoirs: Porosity and diagenesis in a sequence stratigraphic framework, vol 67. Amsterdam, Elsevier

Peterhänsel A, Egenhoff SO (2008) Lateral variabilities of cycle stacking patterns in the Latemar, Triassic, Italian Dolomites. SEPM Spec Publ 89:217–229

Pontiggia M, Ortenzi A, Ruvo L, et al. (2010) New integrated approach for diagenesis characterization and simulation. In: North Africa Technical Conference and Exhibition, Society of Petroleum Engineers

Pyrcz MJ, Deutsch CV (2014) Geostatistical reservoir modeling. Oxford, Oxford university press

Rameil N (2008) Early diagenetic dolomitization and dedolomitization of Late Jurassic and earliest Cretaceous platform carbonates: a case study from the Jura Mountains (NW Switzerland, E France). Sedimentary Geology 212(1-4):70–85

Renard D, Beucher H, Doligez B (2008) Heterotopic bi-categorical variables in pluri-Gaussian truncated simulations. In: Proceedings of the Eighth International Geostatistics Congress Geostats, Citeseer, pp 289–298

Sharp I, Gillespie P, Morsalnezhad D, Taberner C, Karpuz R, Vergés J, Horbury A, Pickard N, Garland J, Hunt D (2010) Stratigraphic architecture and fracture-controlled dolomitization of the Cretaceous Khami and Bangestan groups: an outcrop case study, Zagros Mountains, Iran. Geological Society, London, Special Publications 329(1):343–396

Smith Jr LB (2006) Origin and reservoir characteristics of upper Ordovician Trenton–Black River hydrothermal dolomite reservoirs in New York. AAPG bulletin 90(11):1691–1718

Strasser A (1988) Shallowing-upward sequences in Purbeckian peritidal carbonates (lowermost Cretaceous, Swiss and French Jura Mountains). Sedimentology 35(3):369–383

Strebelle S (2002) Conditional simulation of complex geological structures using multiple-point statistics. Mathematical Geology 34(1):1–21

Taylor KG, Gawthorpe RL, Fannon-Howell S (2004) Basin-scale diagenetic alteration of shoreface sandstones in the Upper Cretaceous Spring Canyon and Aberdeen Members, Blackhawk Formation, Book Cliffs, Utah. Sedimentary Geology 172(1-2):99–115

Taylor TR, Giles MR, Hathon LA, Diggs TN, Braunsdorf NR, Birbiglia GV, Kittridge MG, Macaulay CI, Espejo IS (2010) Sandstone diagenesis and reservoir quality prediction: Models, myths, and reality. AAPG bulletin 94(8):1093–1132

Van Wagoner JC, Mitchum R, Campion K, Rahmanian V (1990) Siliciclastic sequence stratigraphy in well logs, cores, and outcrops: concepts for high-resolution correlation of time and facies. AAPG methods in exploration series, 0743-0531 ; no 7

Vandeginste V, John CM, van de Flierdt T, Cosgrove JW (2013) Linking process, dimension, texture, and geochemistry in dolomite geobodies: A case study from Wadi Mistal (northern Oman) linking process, dimension, texture, and geochemistry in dolomite geobodies. AAPG bulletin 97(7):1181–1207

Verrill AE (1907) The Bermuda islands. part 4, geology and paleontology. Trans Connecticut Academy Arts Sciences 12:316

Wackernagel H (2003) Multivariate geostatistics: an introduction with applications. Berlin, Springer Science & Business Media

Wang L, Wong P, Shibli S, et al. (1998) Modelling porosity distribution in the a'nan oilfield: Use of geological quantification, neural networks and geostatistics. In: SPE International Oil and Gas Conference and Exhibition in China, Society of Petroleum Engineers

White CD, Novakovic D, Dutton SP, Willis BJ (2003) A geostatistical model for calcite concretions in sandstone. Mathematical Geology 35(5):549–575

Wilkinson BH, Drummond CN, Rothman ED, Diedrich NW (1997) Stratal order in peritidal carbonate sequences. Journal of Sedimentary research 67(6)

Table and Figure Captions

Table 1: Proportions of diagenetic facies overprinted on depositional facies in the Latemar carbonate platform, taken from measured sections (Fig. 10).

Table 2: Proportions of diagenetic facies overprinted on depositional facies in the Spring Canyon Member of the Blackhawk Formation, taken from measured sections (Fig. 15).

Figure 1: Four synthetic facies successions: (a) non rhythmic with two cycles; (b) rhythmic (blue facies) with two cycles; (c) cyclic and non rhythmic; and (d) cyclic and rhythmic. Modified from Le Blévec et al. (2018).

Figure 2: Cyclic and rhythmic facies succession (a) with associated transiogram matrix between facies 1 and 2 (b-e). $\overline{L_c}$ is the mean thickness of a facies cycle, and $\overline{L_1}$ and $\overline{L_2}$ are the mean thicknesses of facies 1 and 2. Proportion of facies 1 is 0.5 and proportion of facies 2 is 0.25.

Figure 3: Facies succession (b) modelled with Truncated Gaussian Simulations according to the truncation rule (a) and parameters $r_1 = 0.1$ m , $b_1 = 0$ m^{-1}, $(p_1, p_2, p_3) = (0.4, 0.4, 0.2)$ (Eq. A.4a).

Figure 4: Comparison between conventional Pluri-Gaussian Simulation (PGS) (b) and shifted PGS (c) with the same truncation rule (a). For (b), the parameters are $r_1 = r_2 = 0.6$ m, $b_1 = 15$ m^{-1}, $b_2 = 30$ m^{-1} (Eqs. A.4a, A.4b), and facies proportions $(p_1, p_2, p_3) = (0.5, 0.25, 0.25)$ and for (c), the same parameters are applied together with the shift $\alpha_{12} = 0.04$ m and correlation coefficient $\beta_{12} = -0.7$ (Eq. A.3).

Figure 5: Measured sections through part of the Upper Cyclic Facies interval in the Cimon Latemar outcrop, Latemar platform. Figure modified from Peterhänsel and Egenhoff (2008).

Figure 6: Truncation rule used for modeling depositional facies in the Latemar platform dataset (Fig. 5).

Figure 7: Experimental transiograms (grey points) in the upward vertical direction of depositional facies computed from the measured sections shown in Figure 5,

theoretical transiograms fitted to these points (black line), and transiograms computed in three realizations of the depositional facies Earth model (thin grey lines). The parameters used for the theoretical transiograms are $r_1 = (800, 800, 0.3)$ m, $r_2 = (800, 800, 1.2)$ m, $b_1 = 0$ m^{-1}, $b_2 = 5$ m^{-1}, $\beta_{12} = 0.67$, $\alpha_{12} = 0.1$ m (Eqs. A.4a, A.4b).

Figure 8: Two realizations of an Earth model for depositional facies in the Cimon region of the Latemar carbonate platform conditioned by four measured sections (Fig. 5) with modeling parameters explained in Figures 7.

Figure 9: Three dimensional unconditional realization from a satellite image of Bermuda carbonate platform interior. (a) satellite image (with latitudinal and longitudinal position) showing three types of facies based on visual interpretation: blue represents the lagoon, light green the backreef, and dark green the reef; (b) truncation rule; and (c) 3D Earth model of facies distributions. The parameters of the simulation are $r_1 = r_2 = (20, 100, 0.4)$ m, $\alpha_{12} = (0.1, 5)$ m, $(p_1, p_2, p_3) = (0.15, 0.15, 0.7)$ (Eqs. A.4a, A.4b).

Figure 10: Depositional facies and diagenetic facies in the measured sections through part of the Upper Cyclic Facies in Cimon Latemar outcrop, Latemar carbonate platform (Fig. 5). Measured sections are adapted from Peterhänsel and Egenhoff (2008).

Figure 11: Three dimensional truncation rule used for modeling the depositional facies and diagenetic facies in the Latemar platform dataset (Fig. 10, Table 1).

Figure 12: Experimental vertical cross-transiograms between depositional facies and diagenetic facies (grey points) from measured sections shown in Figure 10, theoretical cross-transiograms fitted to these points (black lines), and cross-transiograms computed in three realizations of a resulting Earth model (thin grey lines). The parameters defining the theoretical transiograms are the same as those for Figure 7, with in addition $\beta_{13} = -0.8$, $\beta_{23} = -0.5$, $\alpha_{13} = -0.1$ m, $\alpha_{23} = 0.1$ m (Eq. A.3).

Figure 13: Experimental transiograms between diagenetic facies (grey points), theoretical transiograms fitted to these points (black lines), and transiograms com-

puted in three realizations of a resulting Earth model (thin grey lines). The parameters defining the theoretical transiograms are the same as those for Figure 7 and 12, with in addition $r_3 = (800, 800, 0.3)$ m and $b_3 = 0$ m^{-1} (Eq. A.4c).

Figure 14: Two realisations of an Earth model for depositional facies and diagenetic facies in the Cimon Latemar region of the Latemar carbonate platform, conditioned by four measured sections with modeling parameters noted in Figure 7, 12 and 13.

Figure 15: measured sections through the Spring Canyon Member, Blackhawk Formation in outcrops of the Book Cliffs, as reported by Taylor et al. (2004), with simplified classification of depositional facies and diagenetic facies, corresponding facies vertical proportion curves, and pie charts of facies proportions in each measured section.

Figure 16: Global truncation rule and two examples of local truncation rules for modeling the Spring Canyon Member, Blackhawk Formation in outcrops of the Book Cliffs. The facies E are depositional facies and D are diagenetic facies.

Figure 17: Two realizations of an Earth model for depositional facies and diagenetic facies in the Spring Canyon Member, Blackhawk Formation, conditioned by nine measured sections with modeling parameters $r_1 = (0.6, 3000, 3000)$ m, $r_2 = (0.7, 3000, 3000)$ m, $r_3 = (1, 1500, 1500)$ m, $b_1 = b_2 = 0$ m^{-1}, $\alpha_{12} = \alpha_{13} = \alpha_{23} = 0$ m, $\beta_{12} = \beta_{13} = \beta_{23} = 0$ (Eqs. A.3, A.4a, A.4b, A.4c).

Figure 18: Uninterpreted (a) and (c); and interpreted (b) and (d) photographs of post-depositional hydrothermal dolomite associated with fractures in the Valsorda valley outcrops of the Latemar carbonate platform. Hydrothermal dolomite confined to the fracture area is shown in red, and hydrothermal dolomite expanding in the host rock is shown in yellow. Modified from Jacquemyn et al. (2014).

Figure 19: (a) Truncation rule and (b) resulting unconditional realization of Earth model of depositional facies (cf. Figure 8) overprinted by post-depositional hydrothermal dolomite diagenetic facies. The parameters used for the simulation are $r_1 = r_2 = (60, 60, 0.2)$ m, $r_3 = (5, 5, 5)$ m, $b_1 = b_2 = b_3 = 0$ m^{-1}, $\beta_{12} = 0.99$,

$\alpha_{12} = 0.1$ m, $\beta_{13} = 0.8$, $\beta_{23} = 0$, $\alpha_{13} = \alpha_{23} = 0$ m (Eqs. A.3, A.4a, A.4b, A.4c).

Table 1:

	Dolomitic crust	**Partial dolomite**
Subtidal	0	0
Intertidal	0	0.10
Supratidal	0	0.02
Exposure	0.32	0

Table 2:

	Carbonate concretion	**White caps**
Distal mudstones	0	0
Shoreface sandstones	0.21	0.03
Foreshore sandstones	0.59	0.4

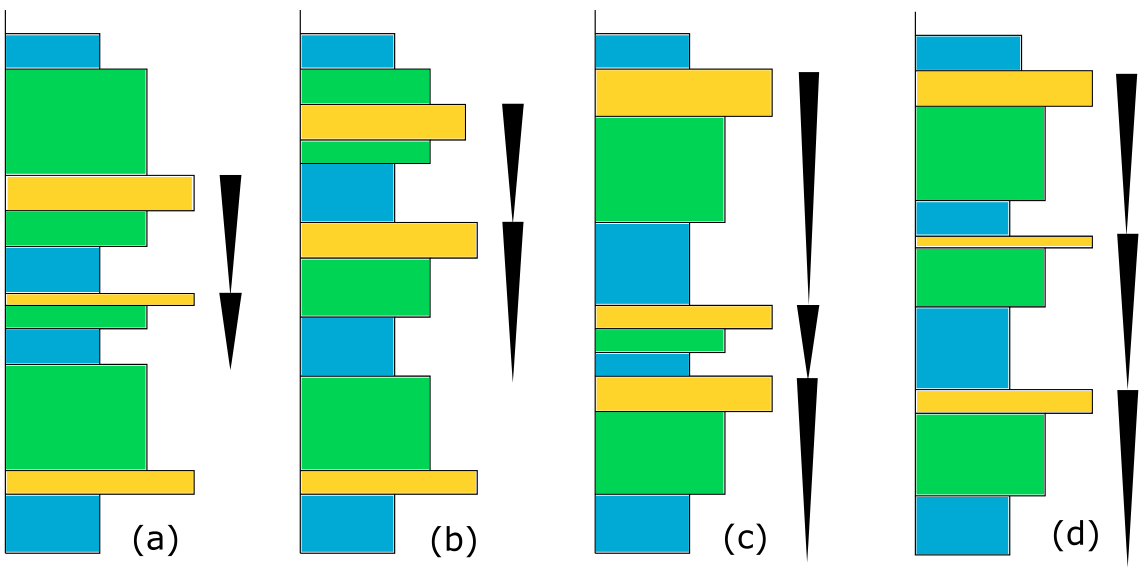

Figure 1:

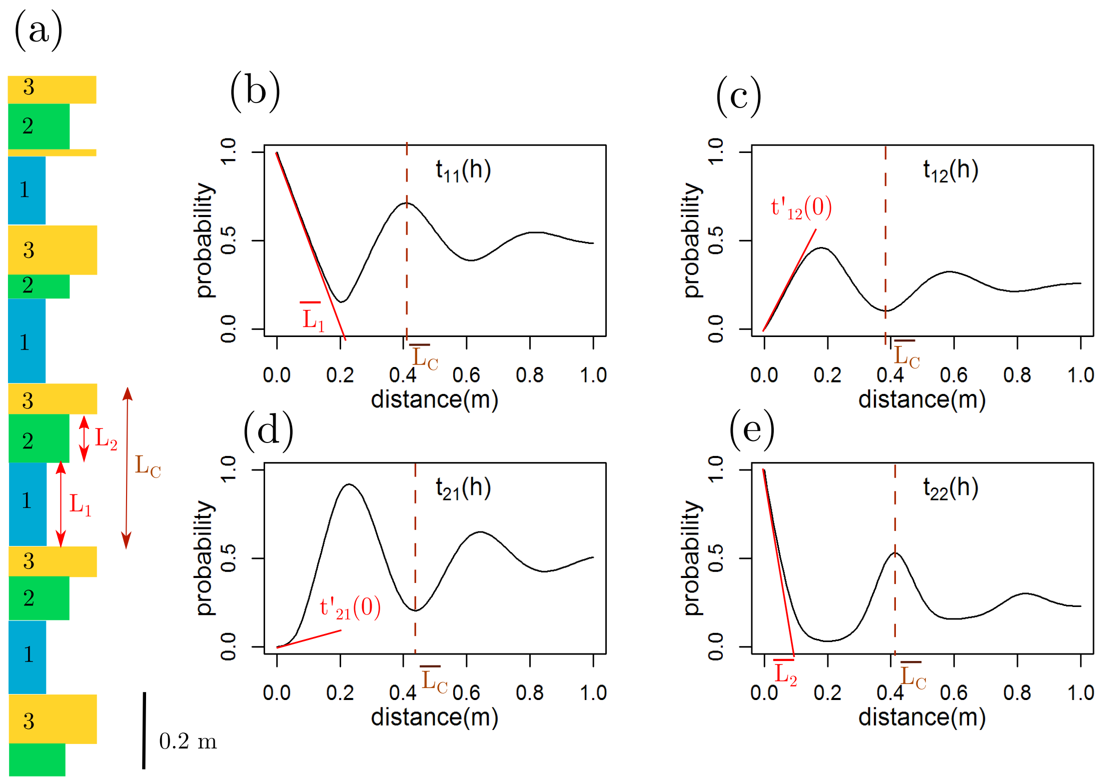

Figure 2:

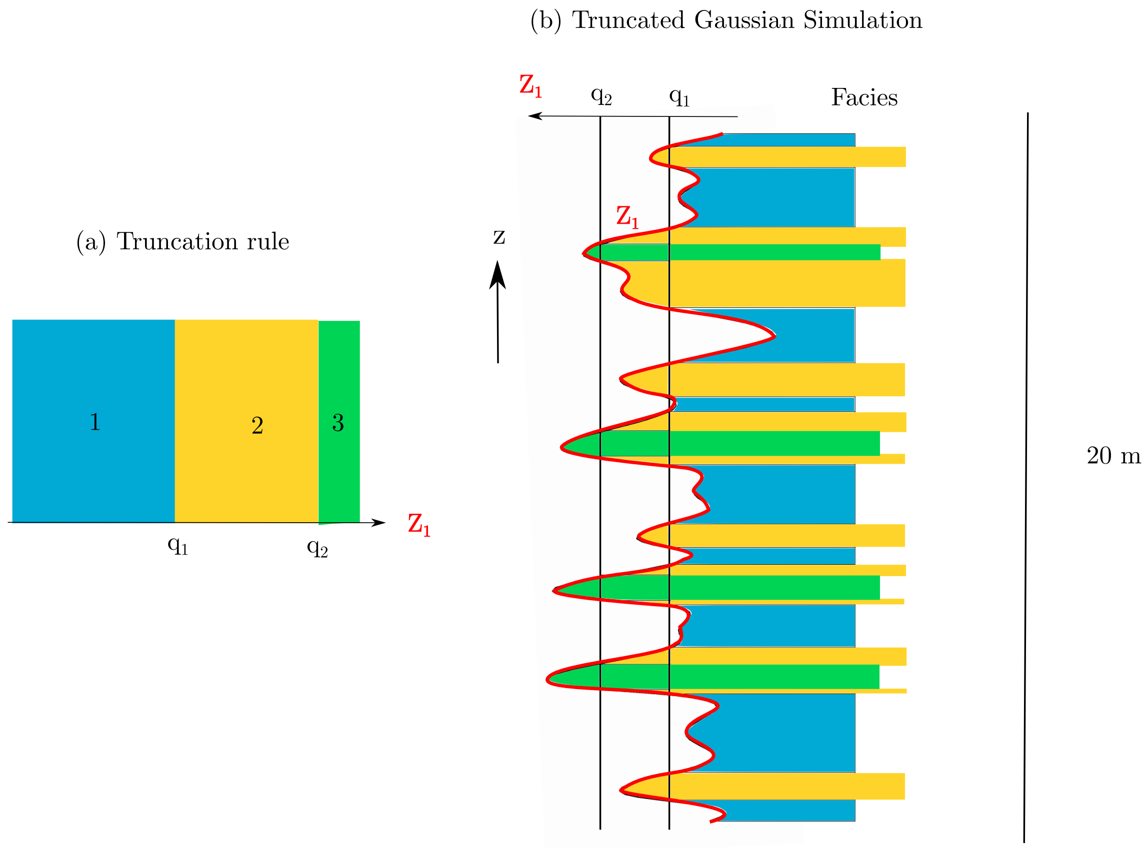

Figure 3:

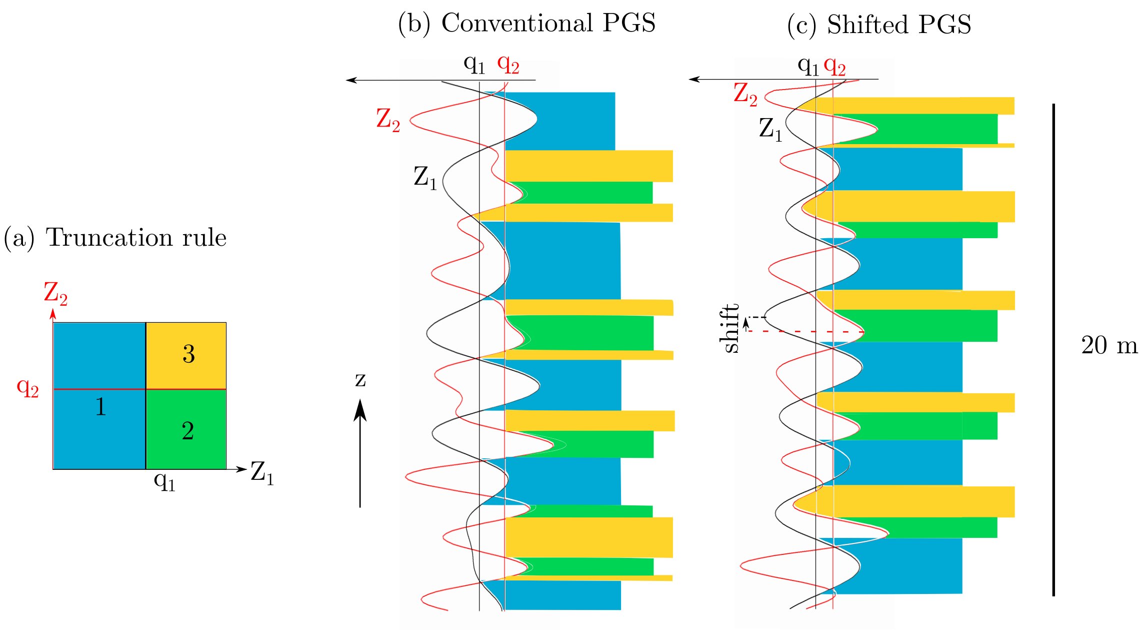

Figure 4:

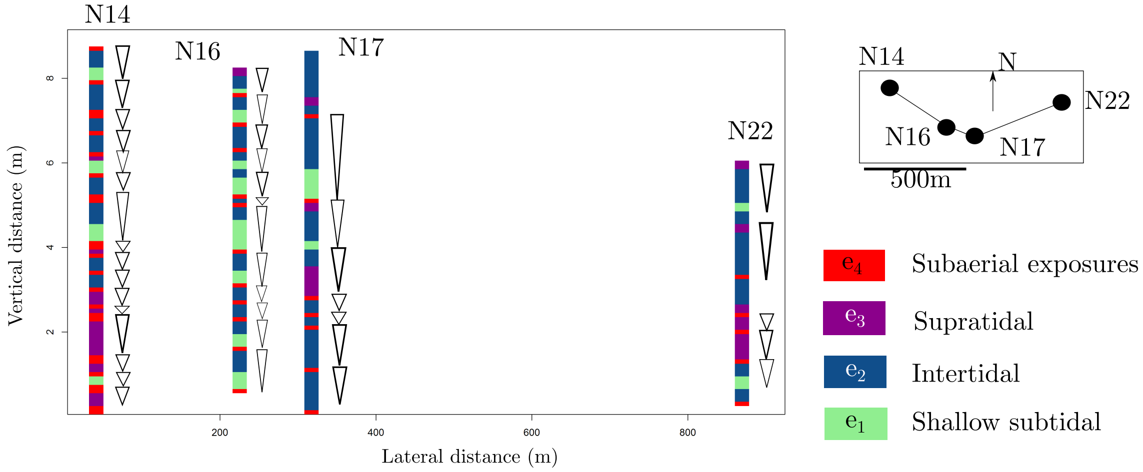

Figure 5:

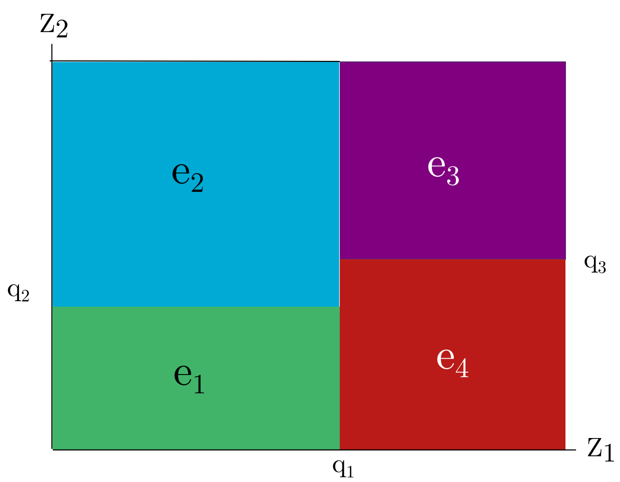

Figure 6:

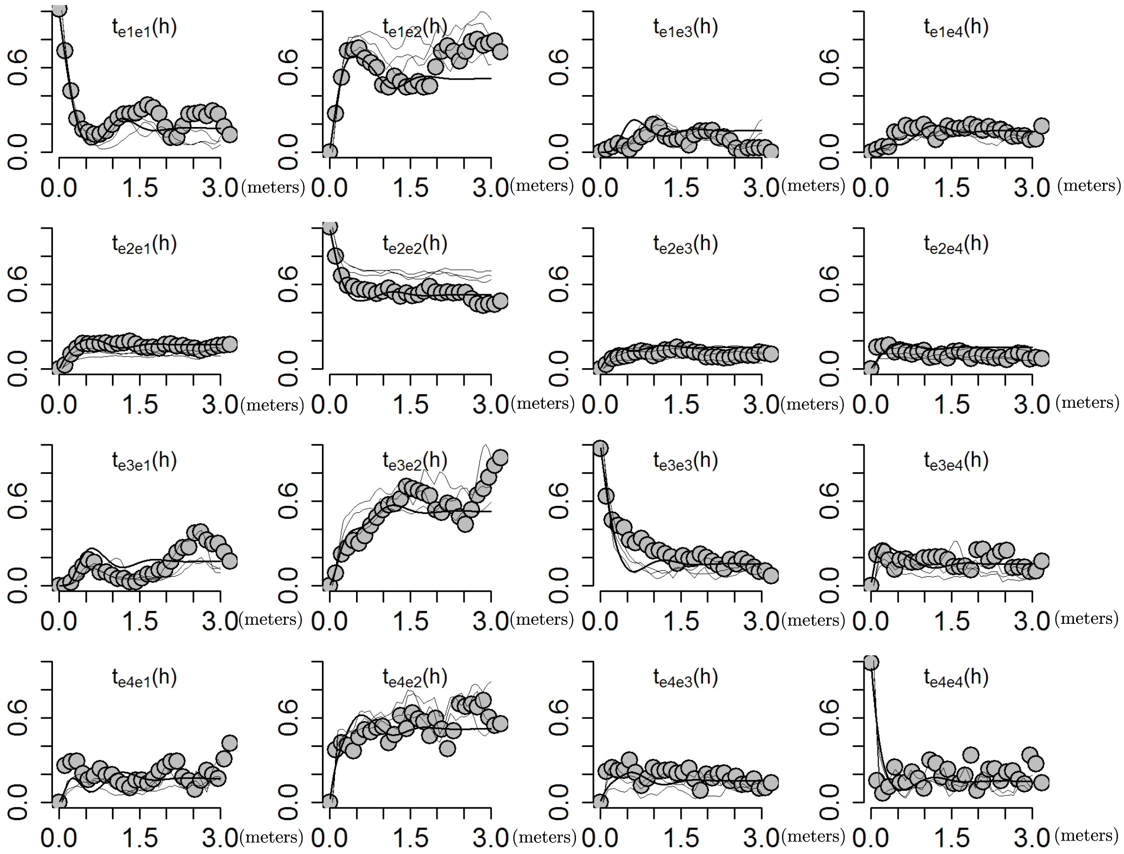

t_{e1e1}(h)
t_{e1e2}(h)
t_{e1e3}(h)
t_{e1e4}(h)
t_{e2e1}(h)
t_{e2e2}(h)
t_{e2e3}(h)
t_{e2e4}(h)
t_{e3e1}(h)
t_{e3e2}(h)
t_{e3e3}(h)
t_{e3e4}(h)
t_{e4e1}(h)
t_{e4e2}(h)
t_{e4e3}(h)
t_{e4e4}(h)
0.0
0.6
0.0
1.5
3.0
(meters)

Figure 7:

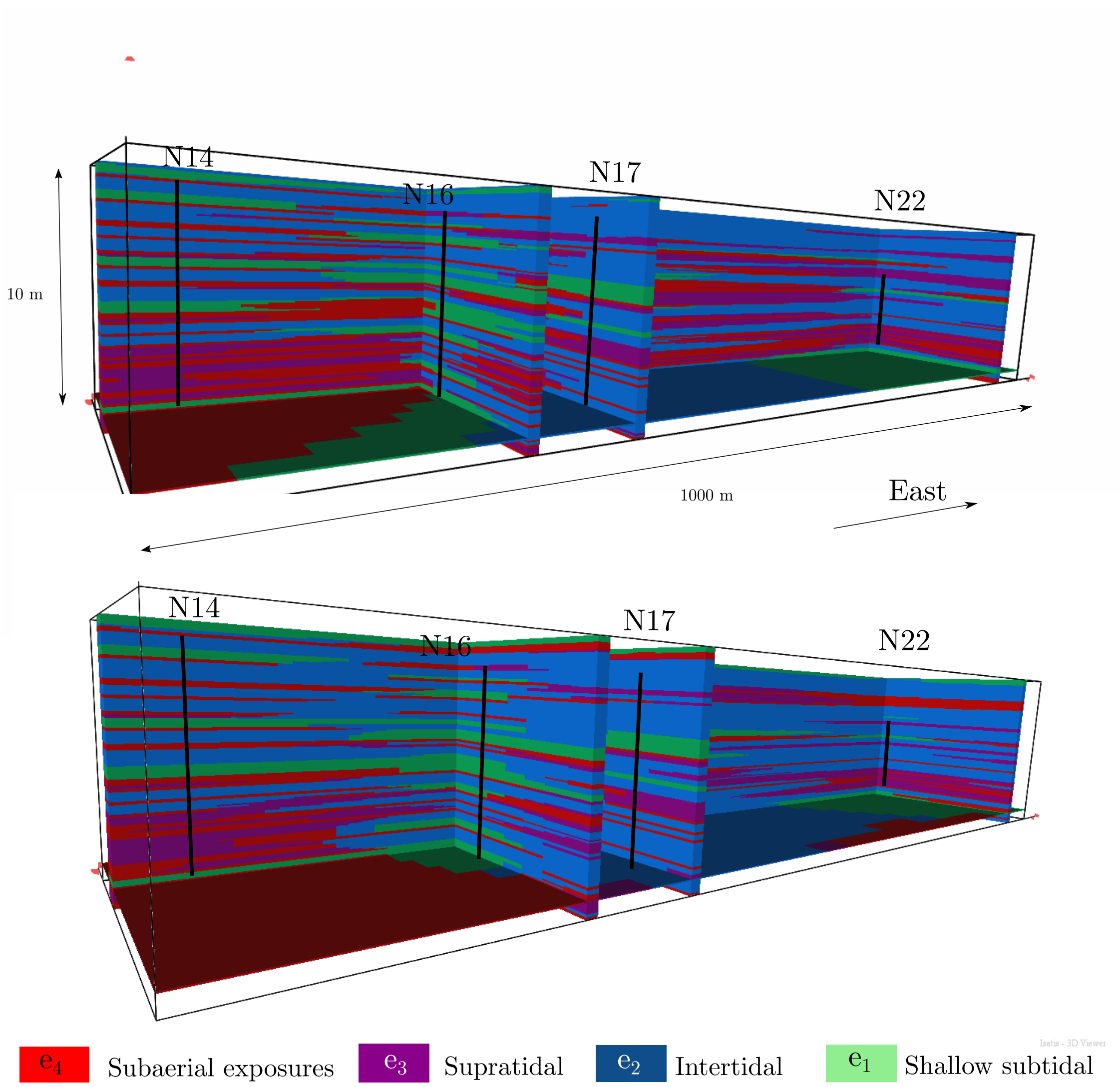

Figure 8:

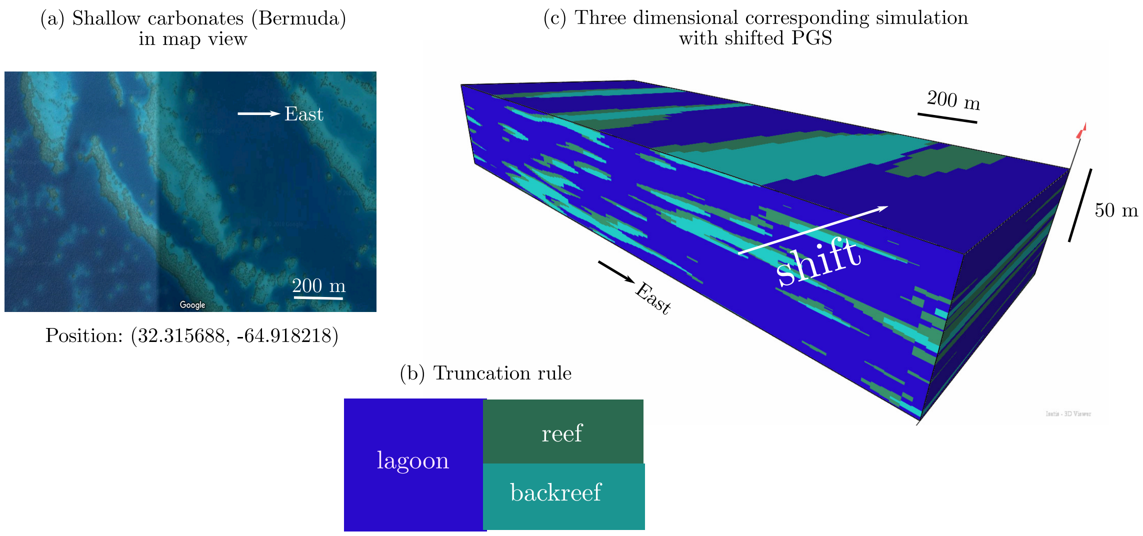

Figure 9:

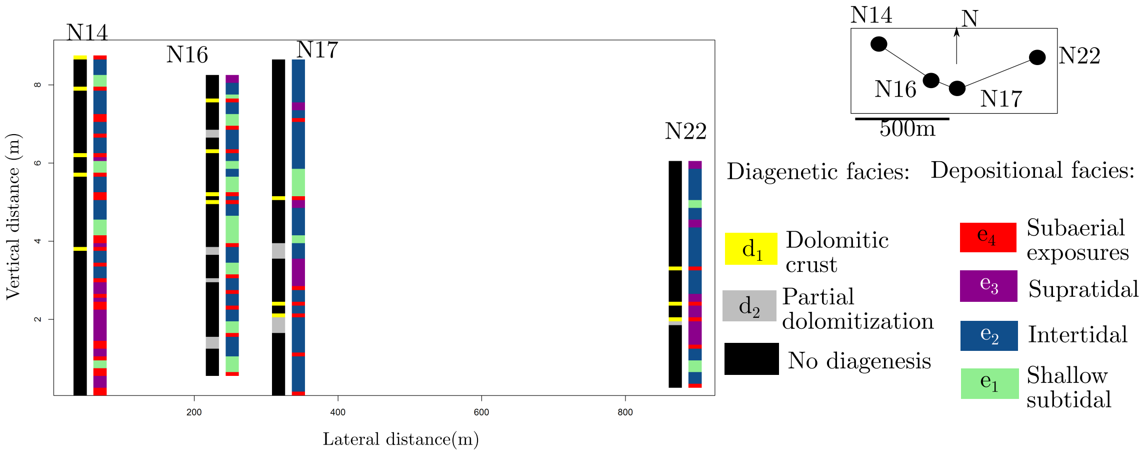

Figure 10:

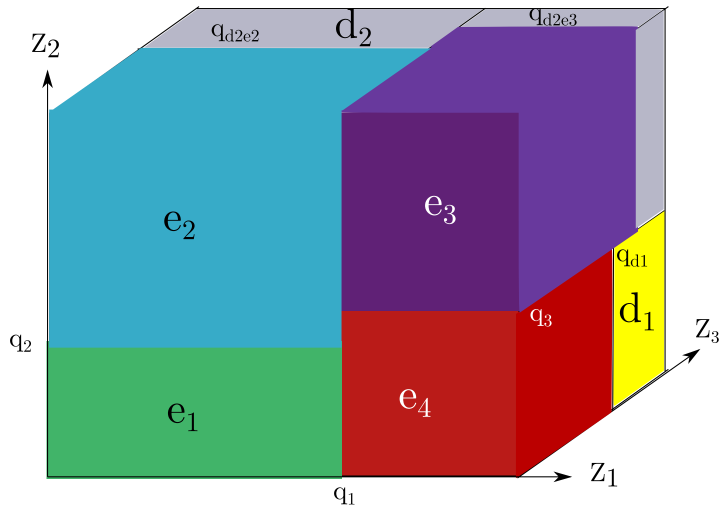

Figure 11:

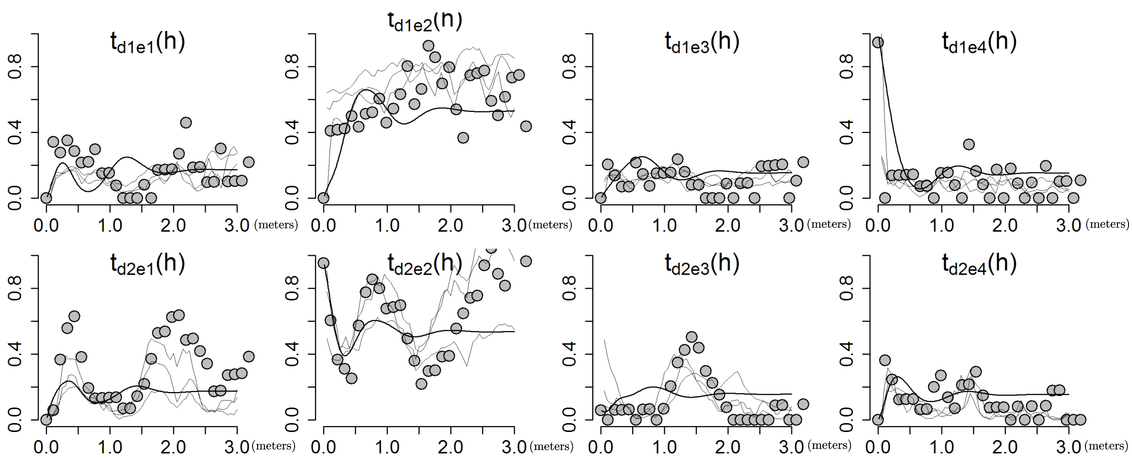

Figure 12:

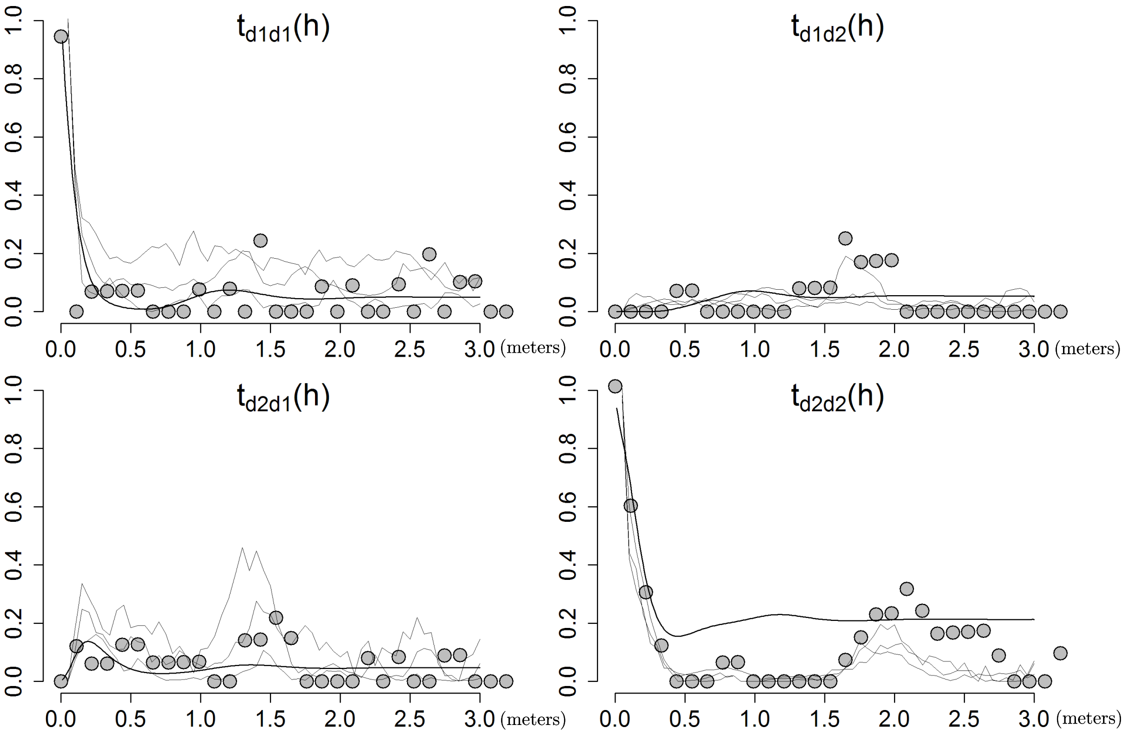

$t_{d1d1}(h)$
$t_{d1d2}(h)$
$t_{d2d1}(h)$
$t_{d2d2}(h)$
0.0
0.2
0.4
0.6
0.8
1.0
0.0 0.5 1.0 1.5 2.0 2.5 3.0 (meters)

Figure 13:

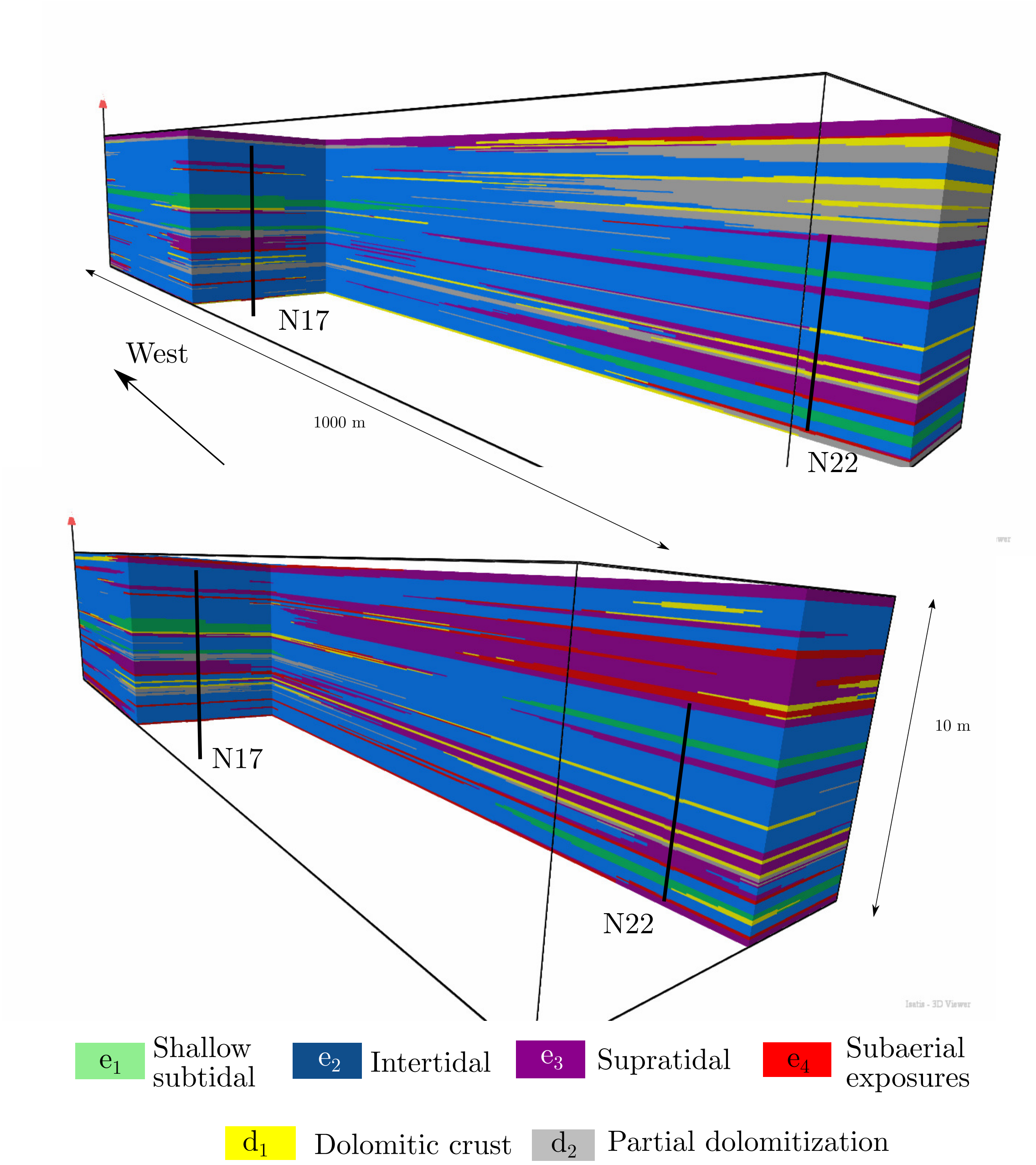
N17
West
1000 m
N22
N17
N22
10 m
e1 Shallow subtidal
e2 Intertidal
e3 Supratidal
e4 Subaerial exposures
d1 Dolomitic crust
d2 Partial dolomitization

Figure 14:

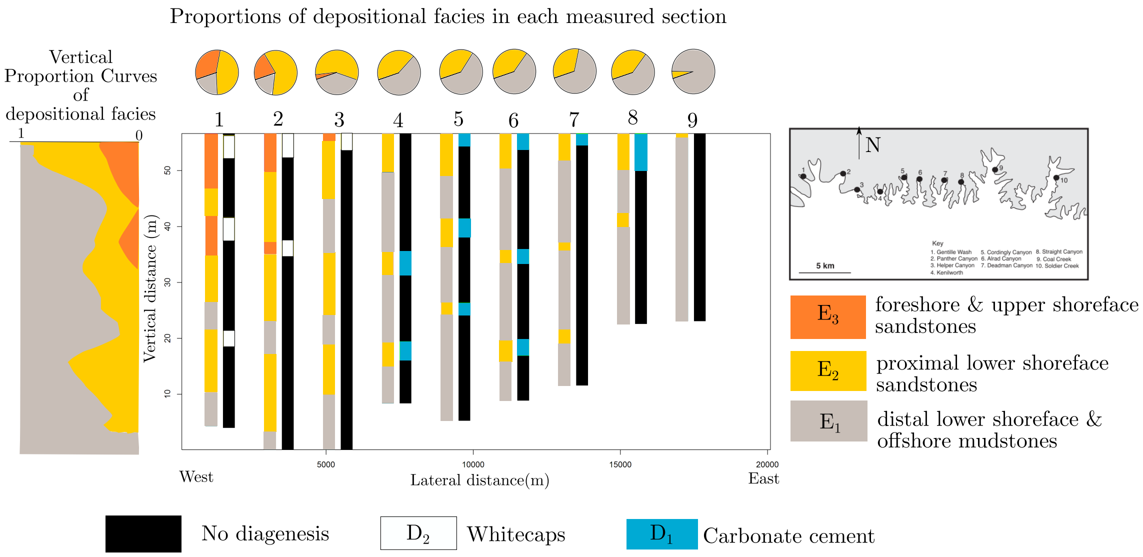

Figure 15:

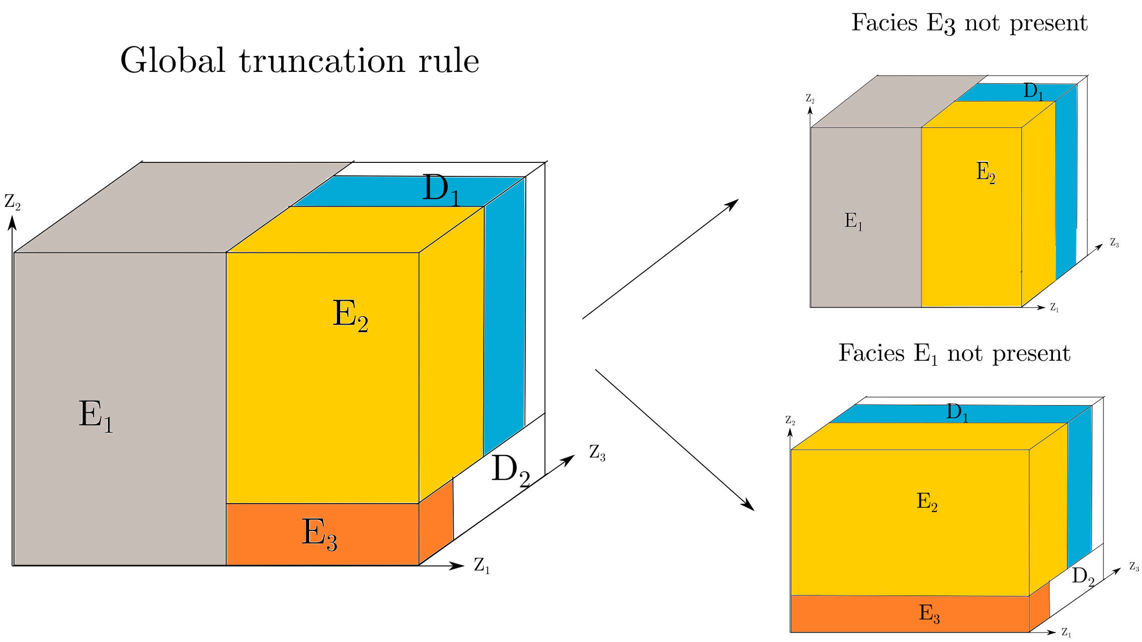

Figure 16:

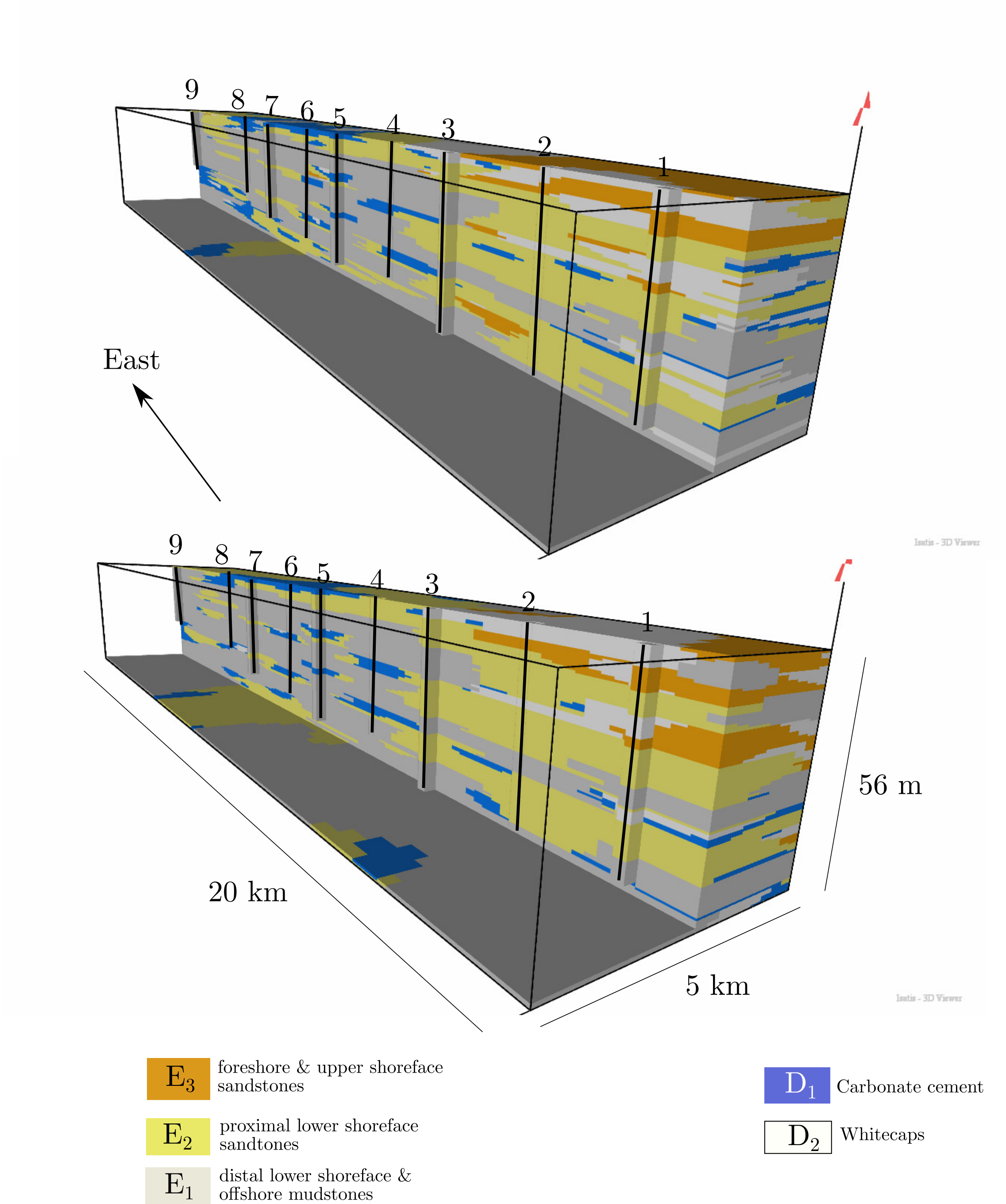
9
8
7
6
5
4
3
2
1
East
20 km
5 km
56 m
E3 foreshore & upper shoreface sandstones
E2 proximal lower shoreface sandtones
E1 distal lower shoreface & offshore mudstones
D1 Carbonate cement
D2 Whitecaps

Figure 17:

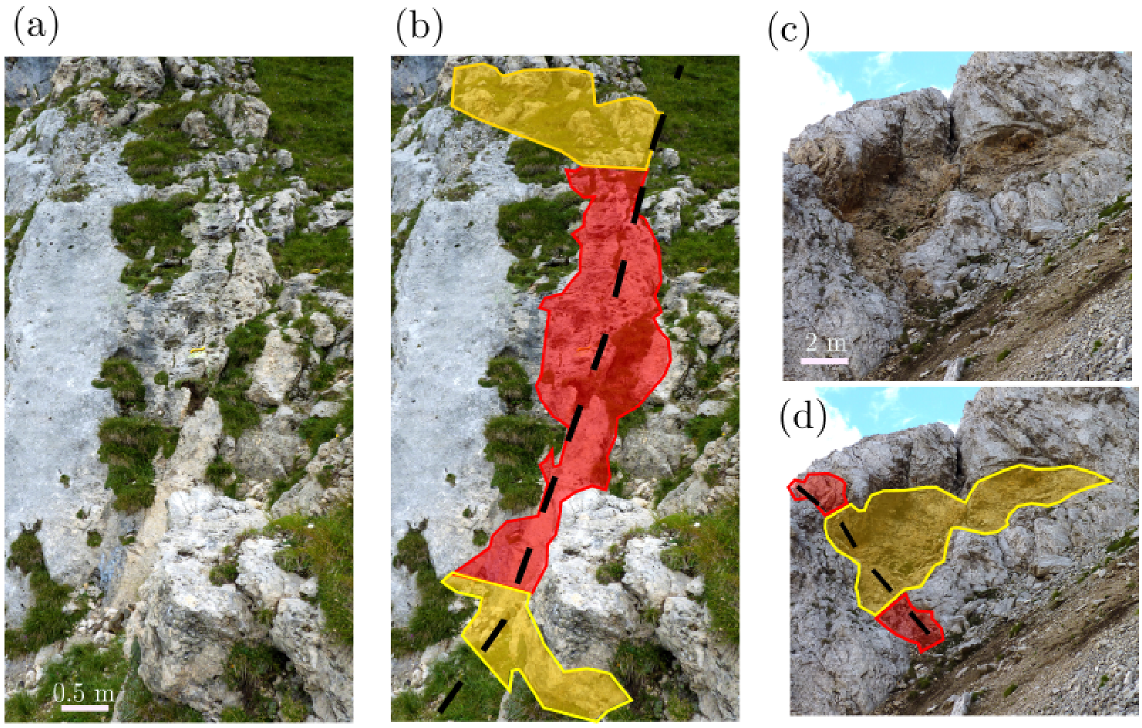

Figure 18:

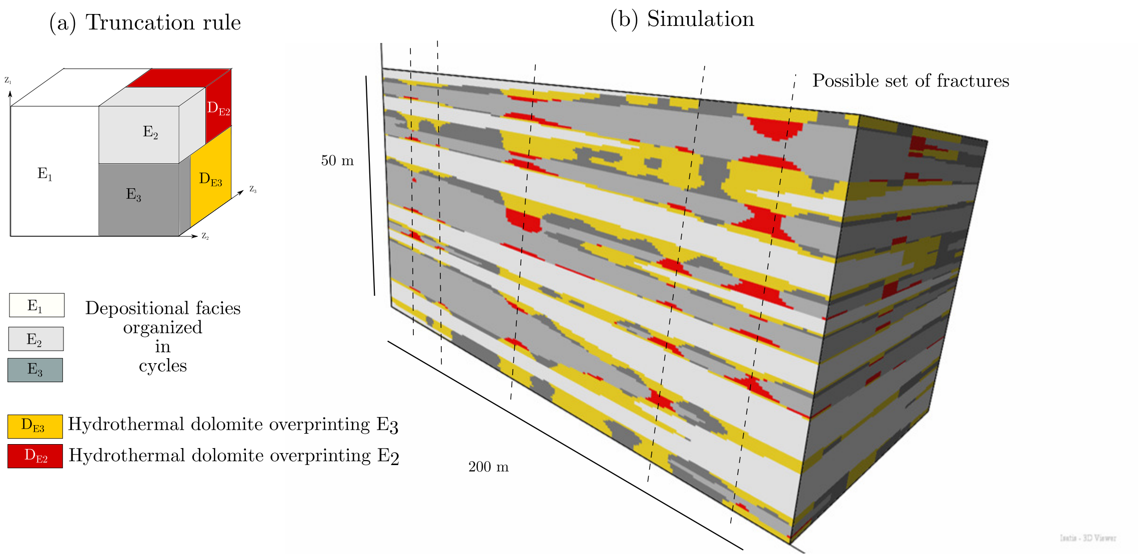

Figure 19: